

Asteroid project summary

JACK T. DINSMORE¹ AND JULIEN DE WIT¹

¹Massachusetts Institute of Technology
Cambridge, MA 02139

ABSTRACT

Abstract.

Keywords: Keywords, em-dash separated

1. INTRODUCTION

- Asteroids simulated in binaries ?
- Previous work on the math of asteroid rotations ??
- CNEOS: 4 asteroids $D > 100m$ are coming to within 1 LD of Earth in the next 10 years, 29 with $D > 10m$.
- Moskowitz survey of Duende: ? with companion observational article ?. Demonstrates that moment of inertia can be extracted from a tumbling asteroid via lightcurve analysis in the zero-torque regime (Fourier transform of lightcurve to pick up on two frequencies and assign precession and nutation frequencies to them.) Assumes constant geometry.
- Study of asteroid binary to extract density ?
- Scheeres theoretical paper ? detailing the different forces and torques felt by an asteroid.
- Paper stating in general that asteroids can be tidally disrupted on hyperbolic flyby. ?, plus similar paper ? for tidal disruption
- Another theoretical paper ? inspired by Paul
- Apophis will definitely pass by Earth and will definitely significantly change its rotation state, but will not undergo tidal disruption. ?

2. ASTEROID MODEL

In an effort to make a general asteroid model, we will consider the entire effect of the tidal torque applied to an asteroid from a planet, rather than solving for the first order perturbation. To better understand the effect, we will not model perturbing effects from other bodies such as the Sun or other planets. However, nearby bodies, such as moons or rings, are considered in a later section. We will also model the asteroid as a rigid body, whose density distribution is fixed throughout the flyby.

Most asteroids are observed to have attained their minimum energy rotation state, so we will also assume that the asteroid's initial state aligns its rotational velocity parallel to the principal axis with maximal moment of inertia.

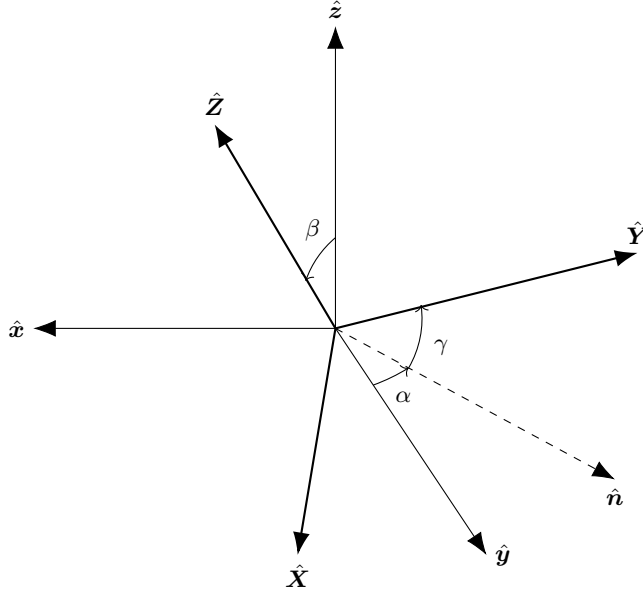


Figure 1. $z - y - z$ Euler angles used in this work to express the orientation of the asteroid. Orientation is expressed as a rotation from the body-fixed axes to the inertial axes.

2.1. Coordinates

We will make use of two frames of reference to model this system. One is the “inertial frame,” with axes denoted by \hat{X} , \hat{Y} , \hat{Z} . As the name suggests, these axes are inertial, with \hat{X} pointing to the asteroid pericenter and \hat{Z} pointing parallel to the orbit angular momentum. The origin of this frame is set to the center of mass of the central body. We will assume that the mass distribution of the central body is known in this inertial frame.

Our second frame is the “body-fixed” frame, denoted by \hat{x} , \hat{y} , \hat{z} . This frame is fixed with respect to the body’s principle axes and rotates with the body, with its origin at the body’s center of mass. We will solve for the asteroid’s mass distribution with reference to the body-fixed frame. For definiteness, we define \hat{z} to be the principal axis with maximal MOI, and \hat{x} to have minimal MOI.

We define a rotation matrix M such that $M\mathbf{r} = \mathbf{R}$, where \mathbf{r} is in the body-fixed frame and \mathbf{R} is in the inertial frame. It will be useful for us to represent this matrix in two different ways; one is with a normalized quaternion $\tilde{\mathbf{q}}$, and the other is with $z - y - z$ Euler angles named α , β , and γ . In particular, we define

$$M = R_z(\alpha)R_y(\beta)R_z(\gamma) \quad (1)$$

where $R_i(\theta)$ is a rotation around the i th unit vector by θ (figure 1).

We use the quaternion $\tilde{\mathbf{q}}$ as our dynamical variable because Euler angles suffer from gimbal lock. For the sake of this paper, we write quaternions as $\tilde{\mathbf{q}} = r + i\mathbf{i} + j\mathbf{j} + k\mathbf{k}$, with the complex conjugate written as $\tilde{\mathbf{q}}^* = r - i\mathbf{i} - j\mathbf{j} - k\mathbf{k}$. The inverse is then $\tilde{\mathbf{q}}^{-1} = \tilde{\mathbf{q}}^*/(\tilde{\mathbf{q}}\tilde{\mathbf{q}}^*)$, and we define real and imaginary parts as $\Re\tilde{\mathbf{q}} = r$; $\Im\tilde{\mathbf{q}} = i\hat{x} + j\hat{y} + k\hat{z}$. See a description of quaternions in Ref. ?

Normalized quaternions express rotations of an angle θ by $\tilde{\mathbf{q}} = \cos \frac{\theta}{2} + \sin \frac{\theta}{2}\tilde{\mathbf{n}}$ where $\tilde{\mathbf{n}} = 0 + n_x\mathbf{i} + n_y\mathbf{j} + n_z\mathbf{k}$. This rotation may be applied to any vector \mathbf{r} by

$$\mathbf{R} = \Im[\tilde{\mathbf{q}}\tilde{\mathbf{r}}\tilde{\mathbf{q}}^{-1}]. \quad (2)$$

Due to the real part of $\tilde{\mathbf{q}}$ which does not vanish for $\theta \rightarrow 0$, quaternions do not suffer from gimbal lock. Using the above notation, we can give the full equation of quaternion multiplication:

$$(q_0 + \tilde{\mathbf{q}})(p_0 + \tilde{\mathbf{p}}) = q_0 p_0 - \mathbf{p} \cdot \mathbf{q} + p_0 \mathbf{q} + \mathbf{q} \times \mathbf{p}. \quad (3)$$

Note that quaternion multiplication is not commutative.

We convert from Euler angles to quaternions by writing equation 1 in terms of quaternions:

$$\tilde{\mathbf{q}} = \begin{pmatrix} \cos \frac{\alpha}{2} \\ 0 \\ 0 \\ \sin \frac{\alpha}{2} \end{pmatrix} \begin{pmatrix} \cos \frac{\beta}{2} \\ 0 \\ \sin \frac{\beta}{2} \\ 0 \end{pmatrix} \begin{pmatrix} \cos \frac{\gamma}{2} \\ 0 \\ 0 \\ \sin \frac{\gamma}{2} \end{pmatrix} = \begin{pmatrix} \frac{\alpha}{2} \cos \frac{\beta}{2} \cos \cos \frac{\gamma}{2} - \frac{\alpha}{2} \cos \frac{\beta}{2} \sin \sin \frac{\gamma}{2} \\ \frac{\alpha}{2} \sin \frac{\beta}{2} \cos \sin \frac{\gamma}{2} - \frac{\alpha}{2} \sin \frac{\beta}{2} \sin \cos \frac{\gamma}{2} \\ \frac{\alpha}{2} \sin \frac{\beta}{2} \cos \cos \frac{\gamma}{2} + \frac{\alpha}{2} \sin \frac{\beta}{2} \sin \sin \frac{\gamma}{2} \\ \frac{\alpha}{2} \cos \frac{\beta}{2} \cos \sin \frac{\gamma}{2} + \frac{\alpha}{2} \cos \frac{\beta}{2} \sin \cos \frac{\gamma}{2} \end{pmatrix}. \quad (4)$$

This equation can be reversed for α, β, γ as follows:

$$\tan \alpha = \frac{jk - ir}{jr + ik} \quad \cos \beta = 1 - 2(i^2 + j^2) \quad \tan \gamma = \frac{jk + ir}{jr - ik}. \quad (5)$$

2.2. Tidal Torque

Derivations for the tidal torque experienced by a rigid body in the gravitational field of a larger mass have been computed by several previous studies ????, sometimes in terms of the moment of inertia of the rigid body (or higher order moments of inertia), and to varying degrees of precision. We present a novel derivation of the tidal torque experienced by a rigid body in a gravitational field of another in terms of (complex) spherical harmonic coefficients of the bodies' mass distributions, which are closely related to their moments of inertia. This formulation of the problem will be more useful for this study. The calculation is performed to all orders of distance between the two bodies.

We start by expressing the gravitational potential energy field of the central body in its most general form:

$$V(\mathbf{R}') = -G \int_{\mathcal{P}} d^3 R \rho_M(\mathbf{R}) \frac{1}{|\mathbf{R} - \mathbf{R}'|}. \quad (6)$$

This integral is computed in the inertial frame and has units of energy per unit mass. We represent the central body density as ρ_M and its volume as \mathcal{P} . To reduce equation 6, we define the unnormalized spherical harmonics $Y_{\ell m}(\theta, \phi) = P_{\ell m}(\cos \theta) e^{im\phi}$, where $P_{\ell m}$ are the associated Legendre Polynomials without the Condon-Shortley phase. The regular and irregular spherical harmonics are then defined as

$$S_{\ell m}(\mathbf{r}) = (-1)^m (\ell - m)! \frac{Y_{\ell m}(\hat{\mathbf{r}})}{r^{\ell+1}} \quad R_{\ell m}(\mathbf{r}) = (-1)^m \frac{r^\ell}{(\ell + m)!} Y_{\ell m}(\hat{\mathbf{r}}). \quad (7)$$

Assume that we can construct a sphere, centered at the center of mass of the central body, so that $\rho_M = 0$ outside the sphere and $\rho_m = 0$ inside the sphere. Then $R' > R$ in equation 6, and Ref. ? gives the identity

$$\frac{1}{|\mathbf{R} - \mathbf{R}'|} = \sum_{\ell, m} R_{\ell m}(\mathbf{R}) S_{\ell m}^*(\mathbf{R}'), \quad (8)$$

where the sum is shorthand for $\sum_{\ell, m} = \sum_{\ell=0}^{\infty} \sum_{m=-\ell}^{\ell}$.

Suppose the vector \mathbf{D} points from the center of mass of the central body to the center of mass of the asteroid, again in the inertial frame. Then we may write $\mathbf{R}' = \mathbf{D} + \mathbf{U}$, and Ref. ? gives

$$S_{\ell m}(\mathbf{R}') = \sum_{\ell', m'} (-1)^{\ell'} R_{\ell' m'}^*(\mathbf{U}) S_{\ell + \ell', m + m'}(\mathbf{D}). \quad (9)$$

Define the complex, unitless constants

$$J_{\ell m} = \int_{\mathcal{P}} d^3 R \rho_M(\mathbf{R}) \frac{R_{\ell m}(\mathbf{R})}{\mu_M a_M^\ell} \quad K_{\ell m} = \int_{\mathcal{A}} d^3 r \rho_m(\mathbf{r}) \frac{R_{\ell m}(\mathbf{r})}{\mu_m a_m^\ell} \quad (10)$$

where the integrals are taken in the inertial and the body-fixed frames respectively. Here, ρ_m denotes the density of the asteroid and \mathcal{A} denotes its volume. The symmetry relations of $R_{\ell m}$ guarantee $J_{\ell m} = (-1)^m J_{\ell, -m}^*$ and similarly for $K_{\ell m}$. We have chosen μ_M, μ_m to be the masses of the central body and asteroid respectively, and a_M and a_m to be scale lengths of both bodies (defined more precisely later). Then we can express the potential as

$$V(\mathbf{U}) = -G \left[\sum_{\ell, m} \mu_M a_M^\ell J_{\ell m} \sum_{\ell', m'} (-1)^{\ell'} R_{\ell' m'}(\mathbf{U}) S_{\ell + \ell', m + m'}^*(\mathbf{D}) \right]. \quad (11)$$

To make use of $K_{\ell m}$ in equation 10, we need to rotate \mathbf{U} from the inertial frame into \mathbf{u} in the body fixed frame via $\mathbf{U} = M\mathbf{u}$. The rotation of a spherical harmonic satisfies

$$Y_{\ell m}(M\mathbf{u}) = \sum_{m'=-\ell}^{\ell} (-1)^{m+m'} \sqrt{\frac{(\ell-m')!(\ell+m)!}{(\ell+m')!(\ell-m)!}} \mathcal{D}_{mm'}^{\ell}(M)^* Y_{\ell m'}(\mathbf{u}). \quad (12)$$

where \mathcal{D} are the Wigner- D matrices. The corollary of this formula for the regular solid spherical harmonic is

$$R_{\ell m}(M\mathbf{u}) = \sum_{m'=-\ell}^{\ell} \sqrt{\frac{(\ell-m')!(\ell+m')!}{(\ell-m)!(\ell+m)!}} \mathcal{D}_{mm'}^{\ell}(M)^* R_{\ell m'}(\mathbf{u}) \quad (13)$$

where $\mathcal{D}_{mm'}^{\ell}$ are the Wigner-D matrix elements. In practice, these are computed from the Euler angles corresponding to the rotation M , which we specified in section 2.1 are $z-y-z$ Euler angles. With this choice of Euler angles, the Wigner-D matrix elements are real with matrix elements given by

$$d_{mm'}^{\ell}(\beta) = \sqrt{(\ell+m)!(\ell-m)!(\ell+m')!(\ell-m')!} \quad (14)$$

$$\sum_{s=\min}^{s=\max} \left[\frac{(-1)^{m-m'+s} (\cos \frac{\beta}{2})^{2\ell+m'-m-2s} (\sin \frac{\beta}{2})^{m-m'+2s}}{(\ell+m'-s)!(\ell-m-s)!(m-m'+s)!s!} \right] \quad (15)$$

where $s_{\min} = \max(0, m' - m)$ and $s_{\max} = \min(\ell + m', \ell - m)$, and $\mathcal{D}_{mm'}^{\ell}(\alpha, \beta, \gamma) = d_{mm'}^{\ell} e^{-im\alpha} e^{-im'\gamma}$.

Combining equations 13 and 11,

$$V(\mathbf{u}) = -G \left[\sum_{\ell,m} \mu_M a_M^{\ell} J_{\ell m} \sum_{\ell',m'} (-1)^{\ell'} S_{\ell+\ell',m+m'}^*(\mathbf{D}) \sum_{m''=-\ell'}^{\ell'} \sqrt{\frac{(\ell'-m'')!(\ell'+m'')!}{(\ell'-m')!(\ell'+m')!}} \mathcal{D}_{m'm''}^{\ell'}(M)^* R_{\ell'm''}(\mathbf{u}) \right]. \quad (16)$$

The tidal torque applied to an asteroid at a point \mathbf{u} is given by $d\boldsymbol{\tau}(\mathbf{u}) = -\rho_m(\mathbf{u}) d^3 u (\mathbf{u} \times (\nabla V_{\mathbf{u}}(\mathbf{u})))$ in the body-fixed frame, which leaves

$$\boldsymbol{\tau} = G \int_A d^3 u \rho_m(\mathbf{u}) \mathbf{u} \times \nabla \left[\sum_{\ell,m} \mu_M a_M^{\ell} J_{\ell m} \sum_{\ell',m'} (-1)^{\ell'} S_{\ell+\ell',m+m'}^*(\mathbf{D}) \right] \quad (17)$$

$$\sum_{m''=-\ell'}^{\ell'} \sqrt{\frac{(\ell'-m'')!(\ell'+m'')!}{(\ell'-m')!(\ell'-m')!}} \mathcal{D}_{m'm''}^{\ell'}(M)^* R_{\ell'm''}(\mathbf{u}) \quad (18)$$

Using the identity

$$\mathbf{u} \times \nabla R_{\ell m}(\mathbf{u}) = \frac{1}{2} [(i\hat{x} - \hat{y})(\ell - m + 1) R_{\ell,m-1}(\mathbf{u})] \quad (19)$$

$$+ (i\hat{x} + \hat{y})(\ell + m + 1) R_{\ell,m+1}(\mathbf{u}) + 2im\hat{z} R_{\ell m}(\mathbf{u}), \quad (20)$$

which was derived from Ref. ?'s analysis of the angular momentum operators applied to spherical harmonics, we write equation 18 as

$$\boldsymbol{\tau} = G \frac{\mu_m \mu_M}{2} \left[\sum_{\ell,m} a_M^{\ell} J_{\ell m} \sum_{\ell',m'} a_m^{\ell'} S_{\ell+\ell',m+m'}^*(\mathbf{D}) (-1)^{\ell'} \sum_{m''=-\ell'}^{\ell'} \sqrt{\frac{(\ell'-m'')!(\ell'+m'')!}{(\ell'-m')!(\ell'+m')!}} \mathcal{D}_{m'm''}^{\ell'}(M)^* \right] \quad (21)$$

$$\left[(i\hat{x} - \hat{y})(\ell' - m'' + 1) K_{\ell',m''-1} + (i\hat{x} + \hat{y})(\ell' + m'' + 1) K_{\ell',m''+1} + 2im''\hat{z} K_{\ell'm''} \right]. \quad (22)$$

This equation contains complex values, but it was numerically confirmed that $\boldsymbol{\tau}$ is a real-valued vector.

Note that each sum in this equation is weighted by a factor of $a_M^{\ell} a_m^{\ell'}/D^{\ell+\ell'+1}$. Since $D \gg a_M \gg a_m$ in general, the leading order torques come from low ℓ and ℓ' . However, $\ell' = 0$ contributes nothing because the inner bracketed term is zero, and $K_{\ell'=1} = 0$ if we choose the origin of the body-fixed axes to be the center of mass of the asteroid. The leading order of equation 22 is therefore $1/D^3$ with $\ell = 0$ and $\ell' = 2$.

2.3. Moment of Inertia

The inertia tensor of the asteroid is expressed as a matrix I . Written in terms of spherical harmonics in the body-fixed frame, we have

$$I = \int_{\mathcal{A}} d^3r \rho_m(\mathbf{r}) \begin{pmatrix} y^2 + z^2 & -xy & -xz \\ -xy & x^2 + z^2 & -xz \\ -xz & -yz & x^2 + y^2 \end{pmatrix} \quad (23)$$

$$= \frac{2}{3} \mu_m a_m^2 \begin{pmatrix} K_{20} - 3K_{2,-2} - 3K_{22} + 1 & 3i(K_{22} - K_{2,-2}) & \frac{3}{2}(K_{21} - K_{2,-1}) \\ 3i(K_{22} - K_{2,-2}) & K_{20} + 3K_{2,-2} + 3K_{22} + 1 - \frac{3}{2}i(K_{21} + K_{2,-1}) & \\ \frac{3}{2}(K_{21} - K_{2,-1}) & -\frac{3}{2}i(K_{21} + K_{2,-1}) & -2K_{20} + 1 \end{pmatrix} \quad (24)$$

where we have defined, for neatness,

$$a_m^2 = \frac{1}{\mu_m} \int_{\mathcal{A}} d^3r \rho_m(\mathbf{r}) r^2. \quad (25)$$

With this definition of a_m , and an arbitrary definition of a_M which may be taken to be similar to equation 25 or a more convenient unit such as the central body radius, the parameters $J_{\ell m}$ and $K_{\ell m}$ of equation 10 are completely defined. Note that a_m is roughly to the radius of the asteroid under certain assumptions; if the asteroid is a sphere of uniform density and radius r , then $a_m = r\sqrt{3/5}$.

Henceforth, we define the body-fixed axis to be coincident with the principal axes of the asteroids, so that the off-diagonal components of I are zero.

2.4. Equation of Motion

As a simplifying assumption, we will not model the effect of the central body's non-sphericity on the asteroid orbit. This effect has been studied in much detail and is small. We therefore separate the position dynamical variables from the angular variables and derive the standard equations of motion for asteroid position in the inertial frame:

$$\dot{\mathbf{V}} = -\frac{G\mu_M}{r^3} \mathbf{D} \quad \dot{\mathbf{D}} = \mathbf{V}. \quad (26)$$

The position variables will no longer be discussed.

Let $\boldsymbol{\omega}$ be the rotational velocity of the asteroid in the body-fixed frame. We have two equations of motion for our system; one governs the evolution of $\boldsymbol{\omega}$ and the other governs the evolution of \mathbf{q} . Starting with the latter, consider a fixed point \mathbf{r} in the body-fixed frame on a rotating asteroid. The corresponding point $\mathbf{R} = \Im[\tilde{\mathbf{q}}\mathbf{r}\tilde{\mathbf{q}}^{-1}]$ in the inertial frame satisfies $\dot{\mathbf{R}} = \Im[\tilde{\mathbf{q}}(\boldsymbol{\omega} \times \mathbf{r})\tilde{\mathbf{q}}^{-1}]$. Furthermore, we can demand that $\boldsymbol{\omega} \perp \mathbf{r}$ so that $\boldsymbol{\omega} \times \mathbf{r} = \Im[\tilde{\boldsymbol{\omega}}\tilde{\mathbf{r}}]$. We obtain another equation for \mathbf{R} by differentiating equation 2 with $\dot{\mathbf{r}} = 0$. Setting these equal,

$$\dot{\tilde{\mathbf{q}}}\tilde{\mathbf{q}}^{-1} + \tilde{\mathbf{q}}\dot{\tilde{\mathbf{q}}}^{-1} = \tilde{\mathbf{q}}\tilde{\boldsymbol{\omega}}\tilde{\mathbf{q}}^{-1}. \quad (27)$$

Substituting $\mathbf{r} \rightarrow \tilde{\mathbf{q}}^{-1}\mathbf{R}\tilde{\mathbf{q}}$ and acknowledging that $\Re[\dot{\tilde{\mathbf{q}}}\tilde{\mathbf{q}}^{-1}] = 0$,

$$\dot{\tilde{\mathbf{q}}}\tilde{\mathbf{q}}^{-1}\mathbf{R} + \mathbf{R}\dot{\tilde{\mathbf{q}}}\tilde{\mathbf{q}}^{-1} = 2\dot{\tilde{\mathbf{q}}}\tilde{\mathbf{q}}^{-1}\tilde{\mathbf{R}} = \tilde{\mathbf{q}}\tilde{\boldsymbol{\omega}}\tilde{\mathbf{q}}^{-1}\mathbf{R}. \quad (28)$$

Since \mathbf{R} is arbitrary, this simplifies to

$$2\dot{\tilde{\mathbf{q}}}\tilde{\mathbf{q}}^{-1} = \tilde{\mathbf{q}}\tilde{\boldsymbol{\omega}}\tilde{\mathbf{q}}^{-1} \Rightarrow \dot{\tilde{\mathbf{q}}} = \frac{1}{2}\tilde{\mathbf{q}}\tilde{\boldsymbol{\omega}}. \quad (29)$$

The second equation of motion are Euler's equations of motion given our expression for tidal torque. Namely,

$$I_1\dot{\omega}_1 - \omega_2\omega_3(I_2 - I_3) = \tau_1 \quad (30)$$

$$I_2\dot{\omega}_2 - \omega_3\omega_1(I_3 - I_1) = \tau_2 \quad (31)$$

$$I_3\dot{\omega}_3 - \omega_1\omega_2(I_1 - I_2) = \tau_3 \quad (32)$$

The components of $\boldsymbol{\tau}$ are given by equation 22, which was also in the body-fixed frame.

2.5. Initial Values

We assume that the asteroid begins the simulation in its minimum energy configuration; that is, with $\omega \parallel \hat{z}$. The initial conditions are therefore that $\omega = \omega\hat{z}$, and the quaternion is fixed to rotate \hat{z} to Ω in the inertial frame, which fixes Euler angles β and α . The third Euler angle γ represents the initial roll of the asteroid, and therefore cannot be determined from physical data. However, it is an initial condition of the simulation. Once the Euler angles are known, the quaternion is computed via equation 4.

2.6. Fit Parameters

By requiring that the $\hat{x}, \hat{y}, \hat{z}$ axes coincide with principal axes, we force the diagonal components of I to be zero. Thus, we may require $K_{21} = K_{2,-1} = 0$ and $\Im K_{22} = \Re K_{2,-2} = 0$ with no loss of generality. By requiring that the body-fixed frame be located at the center of mass of the asteroid, we also require $K_{1m} = 0$. Finally, $K_{00} = 1$ follows automatically from the definition. Thus, K_{20} , $\Re K_{22}$, and $K_{\ell>2,m}$ are the only physical parameters of the asteroid density distribution, beyond a_m .

As discussed before, the leading order of equation 22 is $\ell' = 2$. Therefore, the equation is proportional to $\mu_m a_m^2$. Factoring out this product results in an equation of motion independent of μ_m , meaning that the asteroid dynamics are unaffected by the mass of the asteroid. This is expected, and it means that the density distribution of the asteroid can only be determined up to a scale factor.

Since the coefficient of $J_{lm}K_{l'm'}$ is proportional to $a_M^\ell a_m^{\ell'} / D^{\ell+\ell'+1}$, to first order in the asteroid density distribution, the system is also independent of a_m . When $K_{\ell>2}$ terms are included, a_m scales the size of the higher order terms.

We require that the moment of inertia matrix be positive-definite, which bounds our asteroid parameters. Specifically, we have $K_{20} \leq \frac{1}{2}$, and $|K_{22}| \leq (K_{20} + 1)/6$. We can also choose without loss of generality to let the maximum moment of inertia align with \hat{z} , so that $1 - 2K_{20} \geq K_{20} + 1 + 6|K_{22}|$. Finally, we wish to require that the density of the asteroid be everywhere positive. One consequence of this requirement is that the sum of any two distinct moments of inertia cannot be greater than the third, by the integral definition of moment of inertia in equation 24. Three inequalities result from this, but only one is not covered by the above restrictions. Namely, $I_{xx} + I_{yy} \geq I_{zz} \Rightarrow K_{20} \geq -1/4$. The intersection of these requirements forces K_{20} and K_{22} to lie in the triangle defined by

$$-\frac{1}{4} \leq K_{20} \leq 0 \quad |K_{22}| \leq -\frac{K_{20}}{2}. \quad (33)$$

We have one additional fit parameter, which is the only initial condition not fixed by the problem setup or observations. Namely, the initial value of the first Euler angle α_0 . Due to the fact that the principal axes \hat{x} and \hat{y} are orthogonal, increments of γ_0 by $\pi/2$ correspond to flipping the body-fixed axes so that no physical change in the asteroid model occurs. We must therefore limit the range of γ_0 to width $\pi/2$. Arbitrarily, we choose $\gamma_0 \in [-\pi/4, \pi/4]$

3. EXPERIMENT DESIGN

3.1. Simulation Design

Given the observed orbit of an asteroid and observational data of its resolved spin over time, we built a simulation that would integrate equations 29 and 32 to generate synthetic data. Inputs to the simulation were (1) the ℓ and ℓ' values at which to truncate the potential energy sum in equation 22, (2) the cadence of observations, (3) the J_{lm} parameters and mass and radius of the central body, (4) trial asteroid parameters $K_{\ell m}$, γ_0 and a_m , (5) the initial rotational velocity of the asteroid in the inertial frame, and (6) the asteroid's orbital parameters.

The orbital parameters we use to describe the orbit are the hyperbolic excess velocity v_∞ and the pericenter altitude r_p . The orbit orientation is fixed to lie in the $\hat{X} - \hat{Y}$ plane, with pericenter lying on \hat{X} . The position of the satellite as a function of time is therefore generated by numerically integrating the Newtonian equation of motion (equation 26) from initial values $\mathbf{r}(t=0) = r_p \hat{X}$ and $\mathbf{v}(t=0) = \hat{Y} \sqrt{v_\infty^2 + 2G\mu_M/r_p}$

Once the inputs were specified, the moments of inertia were pre-computed from $K_{\ell m}$, as was the orbital path of the satellite as a function of time. Equations 29 and 32 were then integrated by the Runge-Kutta fourth order method with a time step of *describe* seconds, with a custom implementation of the spherical harmonics and Wigner-D matrices to improve runtime. At fixed time intervals of one cadence, the rotational velocity in the body-fixed frame ω_{xyz} was converted via equation 2 to the inertial frame to produce the synthetic data set.

We begin our simulation at $D = 10r_p$. Since the leading order of the equations of motion is $\ell' = 2, \ell = 0$, this corresponds roughly to a torque of 10^{-3} times the maximum torque at perigee. Unless otherwise indicated, the simulation is terminated at $D = 10r_p$ as well.

3.2. Fitting Method

To analyze the degree to which asteroid density distributions can be determined from flyby rotational velocity data, we use the forward model defined in section 3.1 to generate synthetic data, randomize the data according to one of the observational uncertainty model defined in section 3.3, then use the same forward model to fit to the data and recover parameters.

After randomizing the data, we isolate a set of parameters which are likely to provide good fits. To do this, we minimize the χ^2 value of the data given the model using the Nelder-Mead algorithm, implemented in `scipy`?. Our starting points for the minimization are spaced uniformly randomly across the allowed parameter space, which is the set of parameters with the triangle described by equation 33. The other parameter bounds are $\gamma_0 \in [-\pi/4, \pi/4]$, $|\Re K_{l>2}| \leq 1$, and $|\Im K_{l>2}| \leq 1$.

If the minimization is conducted over too many parameter dimensions, convergence can be slow or can fail. However, the parameters $K_{\ell m}$ are naturally separated into groups by order of ℓ , since the torque applied by successive increment to ℓ is suppressed by a_m/D . Thus, we fit the $\ell = 2$ and γ_0 parameters first, then lock them in place and fit the $\ell = 3$ parameters, etc. The result is a set of points in parameter space which minimize the χ^2 .

Even with this ordering of parameters, the system's strong dependence on asteroid shape makes convergence rare. The data is therefore truncated at distance $D = fr_p$, where f is a manually-set fraction. Once minimization is conducted for the truncated data, the resulting parameters are used as the initial point for a minimization over the entire data set. Experimentation revealed that $f = 2$ was appropriate, where the cut is performed after the perigee for the $\ell = 2$ parameters and before the perigee for the $\ell = 3$ parameters.

We are interested in finding not just the optimal parameters, but the probability distributions of each fit parameter. To do this, we use an Affine Invariant Markov Chain Monte Carlo Ensemble Sampler (MCMC), implemented in the Python package `emcee`, to conduct the fit to data?. This fit method requires the parameter space to be populated with “walkers,” indicating the a guess at the true parameters of the system. We center 32 walkers on the minimizing parameters computed by the minimization of χ^2 , and spread out the walkers such that the number density of walkers is proportional to the likelihood ($\ln \mathcal{L} = -\chi^2/2$) at each point. This is done explicitly by computing the Hessian Σ of the χ^2 value at each minimizing point θ_0 and expressing the likelihood locally as a multi-dimensional Gaussian

$$\mathcal{L}(\boldsymbol{\theta}) \propto \exp\left(-\frac{1}{2}(\boldsymbol{\theta} - \boldsymbol{\theta}_0)^T \Sigma(\boldsymbol{\theta} - \boldsymbol{\theta}_0)\right). \quad (34)$$

We may change bases into a frame in which the parameters are uncorrelated by multiplying by V^T , where V is the matrix of eigenvectors of Σ . Populating the walkers in this uncorrelated space according to Gaussian standard deviations given by the eigenvalues of Σ , we can convert these walkers back to $\boldsymbol{\theta}$ -space by multiplying by V . In practice, we only compute the components of Σ for parameters that are found in the same minimization step; for example, we do not compute the entries of Σ corresponding to K_{20} and K_{30} , setting it equal to zero instead.

Occasionally, the likelihood is non-Gaussian enough for Σ to have negative or otherwise nonsensical eigenvalues (this occurs for strongly varying likelihood or due to numerical errors in the calculation of the Hessian). In these cases, we choose eigenvalues of between *limit* and *limit*.

With the initial walkers distributed, we compute the posterior probability distribution of $\boldsymbol{\theta}$ given flat priors in the range outlined above for each parameter. We run the MCMC until results converge (defined as the condition that the autocorrelation time is less than one hundredth of the current iteration number and that the fractional difference between autocorrelation times is under 1%), or for 100,000 iterations, whichever is smaller. The MCMC is observed only to run for all 100,000 iterations if the data is insufficiently precise to constrain some parameters.

3.3. Uncertainty Models

We model uncertainties in experimental data according to several methods, comparing them to determine the dependence of our conclusions on the sensitivity model used. In every case, the sensitivity model is used both to add randomness to the data set after it is generated, and to weight the χ^2 statistic.

3.3.1. Nominal Method

The most detailed uncertainty model we use, and the one we use most often, is called the “nominal method.” It rotates each angular velocity vector ω by some angle Θ drawn from a normal distribution centered on $\Theta = 0$ with

standard deviation σ_θ . The rotation is done around an arbitrary axis perpendicular to ω . We also allow the length of ω to change by a fraction ρ drawn from a log-normal distribution

$$P(\rho) = \frac{1}{\rho\sqrt{2\pi\sigma_\rho^2}} \exp\left(-\frac{\ln^2 \rho}{2\sigma_\rho^2}\right) \quad (35)$$

so that $\ln\rho$ is normally distributed with mean zero (no change in the length of ω). Both uncertainties σ_θ and σ_ρ are general parameters that can be tweaked to model uncertainty in spin axis direction and period. In our case, we often set $\sigma_\rho = 0$ for simplicity. *Explain why with evidence.*

Practically, the randomization of the data is done by creating a rotation matrix M that rotates $\hat{\mathbf{Z}}$ to the true rotational velocity vector $\boldsymbol{\omega}$. This same rotation matrix is then used to rotate the random vector $\boldsymbol{\Omega} = \rho\omega(\sin\Theta\cos\Phi\hat{\mathbf{X}} + \sin\Theta\sin\Phi\hat{\mathbf{Y}} + \cos\Theta\hat{\mathbf{Z}})$ to the randomized velocity vector. Here, Φ is a uniformly random variable in the range $[0, \pi]$. Specifically, we write this matrix as

$$M = \rho \begin{pmatrix} \cos\phi & -\sin\phi & 0 \\ \sin\phi & \cos\phi & 0 \\ 0 & 0 & 1 \end{pmatrix} \begin{pmatrix} \cos\theta & 0 & \sin\theta \\ 0 & 1 & 0 \\ -\sin\theta & 0 & \cos\theta \end{pmatrix} \quad (36)$$

where θ and ϕ are the spherical coordinates of the original velocity vector $\boldsymbol{\omega}$.

Equation 36 is sufficient to randomize synthetic data, but an analytical expression for the coordinates of $\boldsymbol{\omega}$ is required to define the χ^2 value used for fitting. We approximate the distribution of each spin coordinate as normal, with covariance given by the covariance of the true distribution. Based on equation 36, the covariance matrix is

$$\text{Cov}(\boldsymbol{\omega}) = \frac{1}{2} e^{-\sigma_\theta^2+2\sigma_\rho^2} \left[\left(e^{-\sigma_\theta^2} - 2e^{-\sigma_\rho^2} + \cosh(\sigma_\theta^2) \right) \begin{pmatrix} \omega_x^2 & \omega_x\omega_y & \omega_x\omega_z \\ \omega_x\omega_y & \omega_y^2 & \omega_y\omega_z \\ \omega_x\omega_z & \omega_y\omega_z & \omega_z^2 \end{pmatrix} + \sinh(\sigma_\theta^2) \mathbb{1} \right]. \quad (37)$$

The difference between this Gaussian approximation and the true distribution are shown in figure 2 (a), which shows the distribution of the components of 10^5 angular velocity vectors and their correlations, randomly generated for a true velocity vector given by the reference value (appendix A), both using the true uncertainty method and the Gaussian approximation. The true distribution is more likely to yield results close to the true value than the Gaussian approximation. Agreement also worsens in the case where one of the components of ω nears zero (not shown). This may have the result of our likelihood not perfectly representing our system, and the fit probabilities will be slightly inaccurate.

A larger source of disagreement between the Gaussian approximated likelihood and the true distribution is the correlation between all three components of ω . If two components of ω , the third component is known up to its sign except when $\sigma_\rho \neq 0$. However, the covariance matrix of $\boldsymbol{\omega}$ does not capture this, nor do the distributions displayed in figure 2 (a). Therefore, when $\sigma_\rho \simeq 0$, the Gaussian likelihood function may poorly represent the model. To demonstrate this, we show a histogram of the norm of ω for the Gaussian approximated distribution and the true distribution in figure 2 (b), which demonstrates that statistics involving all three components of $\boldsymbol{\omega}$ can differ highly between the approximation and the true distribution.

Aware of the failings of the Gaussian likelihood assumption, we then define the χ^2 statistic to be

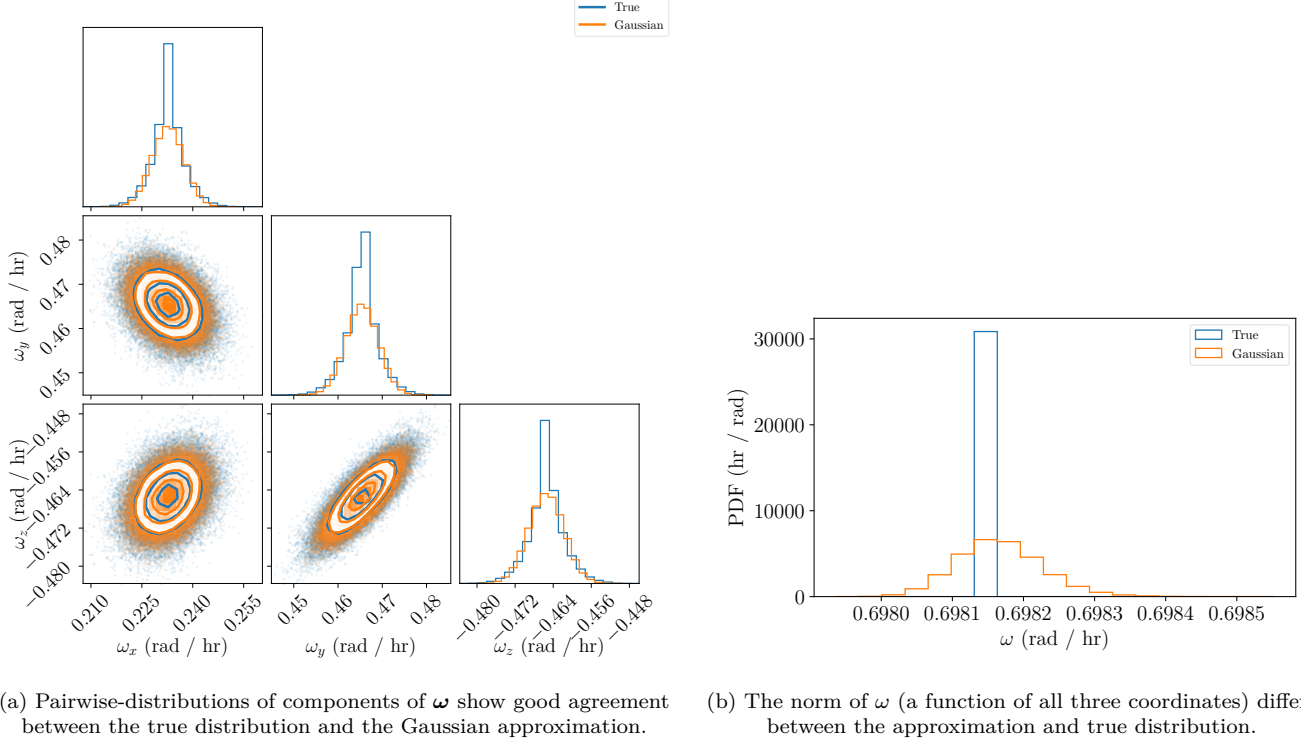
$$\chi^2 = \sum_{i=0} (\boldsymbol{\omega}_i^* - \boldsymbol{\omega}_i)^T \text{Cov}^{-1}(\boldsymbol{\omega}_i^*) (\boldsymbol{\omega}_i^* - \boldsymbol{\omega}_i) \quad (38)$$

where $\boldsymbol{\omega}_i$ is the i th expected spin and $\boldsymbol{\omega}_i^*$ is the data. We also refer to the reduced chi squared, $\chi_r^2 = \chi^2/(3N)$, where N is the number of $\boldsymbol{\omega}_i$ in the data set.

All this text is explanatory material for what I've been doing, but in the paper only the true likelihood will be there probably.

Given the above explanation of the nominal uncertainty method, we define the likelihood of our data to be

$$\ln \mathcal{L} = \sum_{i=0} -\frac{\cos^{-1}(\boldsymbol{\omega}_i^* \cdot \boldsymbol{\omega}_i)^2}{2\sigma_\theta^2} - \frac{\ln(\omega_i^*/\omega_i)^2}{2\sigma_\rho^2} - \ln \frac{\omega_i^*}{\omega_i}. \quad (39)$$



(a) Pairwise-distributions of components of ω show good agreement between the true distribution and the Gaussian approximation.

(b) The norm of ω (a function of all three coordinates) differs between the approximation and true distribution.

Figure 2. The true distribution (blue) and the Gaussian approximation (orange) with the same covariance (orange) for the components of angular velocity ω under the nominal uncertainty method.

Sometimes we compute the value $\chi^2 = -2 \ln \mathcal{L}/N$ where N is the number of spin vectors in the data set. For uncorrelated uncertainty *Check the assumptions on which the chi squared distribution is met* we expect $\chi^2 \approx 1$ for large N . However, due to the highly correlated nature of our data, this limit occurs in our data set.

In figure 3 we present example data for this asteroid using the two reference asteroid and orbit parameters described in appendix A. Additionally, one thousand simulations are also run with asteroid parameters γ_0 , K_{20} , and K_{22} changed slightly, distributed according to the likelihood defined by equation ?? with this nominal uncertainty method and $\sigma_\theta = 0.2$. The method for distributing these shape parameters is the same as the method for distributing the MCMC initial walker positions, described in section 3.2. Bands containing 68.3%, 95.5%, and 99.7% of these additional simulations are also plotted in figure 3.

3.3.2. Position dependent method

In practice, precision on the asteroid spin axis will increase with decreasing distance *Citation needed*. The nominal sensitivity model does not account for this; however, we can approximate this effect by choosing σ_θ from the nominal method to be position-dependent. Specifically, we choose

$$\sigma_\theta(D) = \text{unimplemented}. \quad (40)$$

We do not expect this change to differ qualitatively from the nominal method because resolution is most important near pericenter, where D is stationary to first order.

3.4. System Setup

We study several environments for our asteroid, including (1) a flyby of a single, spherical planet, (2) a close flyby of a ringed planet, (3) a flyby of a planet with a moon, and (4) a close flyby of a planet with a moon. The qualitative and quantitative differences between these flyby types are discussed below.

3.4.1. One Spherical Planet

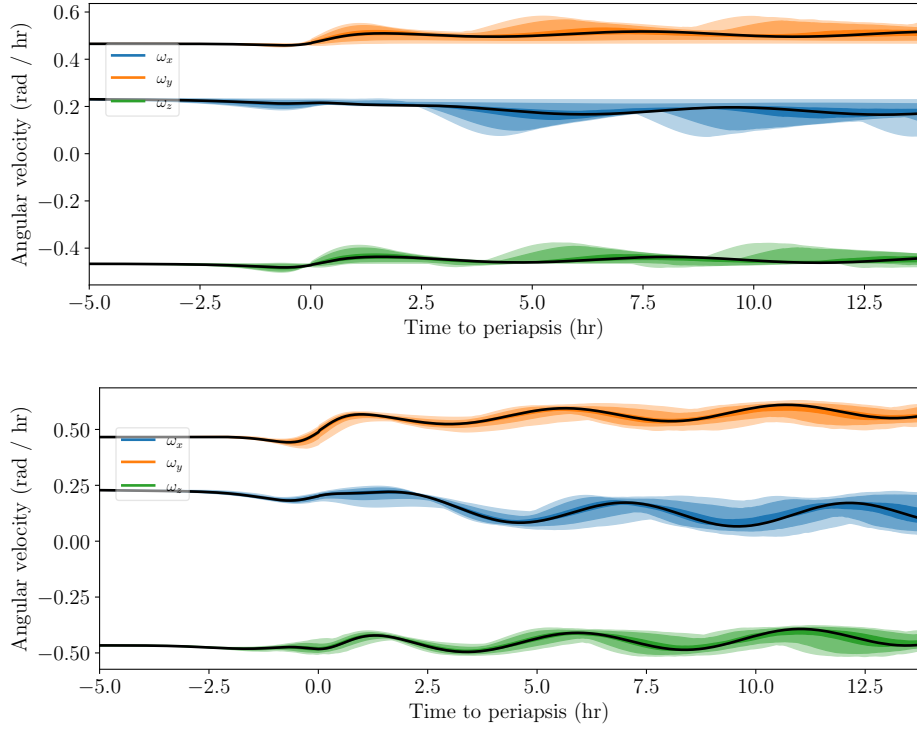


Figure 3. Angular velocity data simulated for the symmetric (above) and asymmetric (below) reference asteroid densities and the reference orbit (black lines). Also plotted is the deviation of the data for likelihood-distributed changes to the asteroid shape (bands) using the nominal uncertainty method. Bands contain 68.3%, 95.5%, and 99.7% of the 1000 simulations run.

The simplest setup for an asteroid flyby is a close flyby of a single, spherical body. We call this central body a “planet” because it is likely that a body massive enough to observably torque an asteroid would be a planet. For such a body, the only relevant physical parameter is its mass, μ_M , since $J_{00} = 1$ and the other $J_{\ell m}$ parameters are zero.

3.4.2. Ringed Planet

Equation 22 demonstrates that parameters controlling non-sphericity in the central body (J_{2m} , J_{3m} , etc.) are damped by a factor of $(a_M/D)^\ell$, where a_M can be thought to be the radius of the central body. Furthermore, the J_{1m} terms are all zero by choosing the center of mass of the central body to be the origin of the coordinate system. Thus, we are interested in the extreme values of $J_{\ell \geq 2}$ and whether they have a significant effect on the observability of asteroid density distributions. An example of such an extreme value is the presence of a planetary ring.

For a ring of inner radius a , outer radius b , and mass μ_r oriented in the $\hat{\mathbf{X}} - \hat{\mathbf{Y}}$ plane, the only changed $J_{\ell m}$ s have $m = 0$ by rotational symmetry. Furthermore, $Y_{\ell,m} = 0$ on the equator for odd m , and $(-1)^{\ell/2} \ell! / (2^\ell (\ell/2)!^2)$ otherwise. Thus, we have

$$J_{\ell m} = \begin{cases} \frac{2\pi\sigma}{\mu_M + \pi(b^2 - a^2)\sigma} \frac{(-1)^{\ell/2}}{a_M^\ell} \frac{b^{\ell+2} - a^{\ell+2}}{2^\ell (\ell/2)!^2 (\ell+2)} & \text{for } m = 0, \ell \text{ even, } \ell \neq 0 \\ 1 & \ell = 1 \\ 0 & \text{else} \end{cases} \quad (41)$$

where μ_M is the mass of the planet without the ring and σ_s is the surface density of the ring.

The oblateness ϵ , also called J_2 of a body is defined as $\epsilon = (I_z - I_x)/(\mu_M a_M^2)$, where $I_x = I_y$ (that is, $J_{22} = 0$) and a_M is the true radius of the body, not the value defined in equation 25. Expressed in terms of $J_{\ell m}$, this is $\epsilon = -2J_{20}$. We can compare typical oblateness to the J_{20} value from equation 41 to see which effect is more dramatic.

Using data from the NASA Saturn Fact Sheet, we arrive at $J_{20} \sim 10^{-8}$ from rings, but 10^{-4} from oblateness. So oblateness is in fact the stronger effect.

Don't actually use this section in the paper. I'm keeping it here as a math repository. Change the section to an oblate planet.

3.5. Planet with a Moon: Distant Flyby

Consider a system with a moon of mass μ_o at constant displacement \mathbf{R} from the central body. We assume that both the planet and the moon are spherical. As long as the distance from the barycenter of the planet-moon system to the asteroid D always satisfies $D > r$ we are free to use the formalism developed above, absorbing the moon into $J_{\ell m}$. Making use of the identity ?

$$R_{\ell m}(\mathbf{R} + \mathbf{R}') = \sum_{\ell'=0}^{\ell} \sum_{m'=-\ell'}^{\ell} R_{\ell' m'}(\mathbf{R}') R_{\ell-\ell', m-m'}(\mathbf{R}) \quad (42)$$

Is this true? for $R > R'$, we have

$$J_{\ell m} = \frac{1}{(\mu_M + \mu_0)a_M^\ell} \left[\delta_{\ell 0} \delta_{m 0} \mu_M + \int_{\mathcal{P}} d^3 r' \rho_o(\mathbf{r}') R_{\ell m}(\mathbf{R} + \mathbf{r}') \right] \quad (43)$$

$$J_{\ell m} = \frac{1}{(\mu_M + \mu_0)} \left[\mu_M \delta_{\ell 0} \delta_{m 0} + \mu_o \frac{R_{\ell m}(\mathbf{R})}{a_M^\ell} \right] \quad (44)$$

where the δ s are Kronecker deltas. It is apparent that if a_M^ℓ remains the radius of the planet, $|J_{\ell m}| \rightarrow \infty$ as $\ell \rightarrow \infty$. However, since each $J_{\ell m}$ is damped by a_M^ℓ/D^ℓ and since $R < D$ by construction, the series in equation 22 remains roughly geometric and does not blow up. For the sake of this calculation, we neglect motion of the moon during the flyby.

For our tests, we use parameters similar to our Moon: we set $\mu_o = 0.01\mu_M$ and $R = 60a_M$.

3.6. Planet with a Moon: Close Flyby

If, contrary to the previous section, we want to fly by both the moon and the planet of a binary system, we must consider the tidal torque contributions from both bodies separately. The formalism above cannot be extended to write one set of $J_{\ell m}$ for both the moon and planet. To do this, we generate two separate paths of $\mathbf{D}(t)$, one pointing from the central body to the asteroid and one pointing from the moon to the asteroid. Both are defined in the inertial reference frames. Then the torque from both can be computed by equation 22 and added to get the net torque on the asteroid. Again, we neglect motion of the moon during the flyby.

4. RESULTS

To interpret the capacity of this tidal torque technique to constrain the density distribution of asteroids, we generate synthetic data in multiple simulated settings and fit to this data using an MCMC, reporting the standard deviation of the posterior parameter distributions as a measure of the effectiveness of the fit. Fits with narrow posterior distributions are considered more effective than those with wide posterior distributions, and the correlations between parameters are also of interest when computing uncertainties on physical models for the asteroid shape.

The distributions are nearly Gaussian in most cases (see appendix ??) and all fits are run until convergence.

4.1. Dependence on asteroid parameters

Of first importance is the dependence of parameter uncertainties on the true parameter values. To measure this, we run 120 fits, all for the two $K_{\ell=2}$ parameters and γ_0 with the standard orbit (appendix ??) and experimental uncertainty $\sigma_\theta = 0.01$ with the nominal uncertainty model (section 3.3). Each fit is run for $\gamma_0 = \pi/8$ and K_{20}, K_{22} distributed in a triangular lattice with 17 layers, spanning the parameter space. The 33 cases with extremal values of K_{22} are not fitted as being too close to the edge of the parameter space.

The parameters K_{22} and K_{20} are then converted to the more physical parameters a/c and b/c under the assumption of an elliptical asteroid of uniform density with minor axes a, b, c (section 5.1.1). Uncertainties on γ_0 and the two shape parameters are given in figure 4, and correlations between pairs of parameters ($\text{Corr}(X, Y) = \text{Var}(X, Y)/(\sigma_X \sigma_Y)$) are given in figure 5.

These figures demonstrate several key properties. Figure 4 demonstrates that fit uncertainties for all three parameters are generally for asteroids with an axis of rotational symmetry — i.e. $a = b$ or $K_{22} = 0$. This is likely due to the fact that the local axes, which are required to define the parameters, are set such that they align with the asteroid principal axes, and therefore are degenerate in the case of a symmetrical asteroid. For similar reasons, uncertainty in

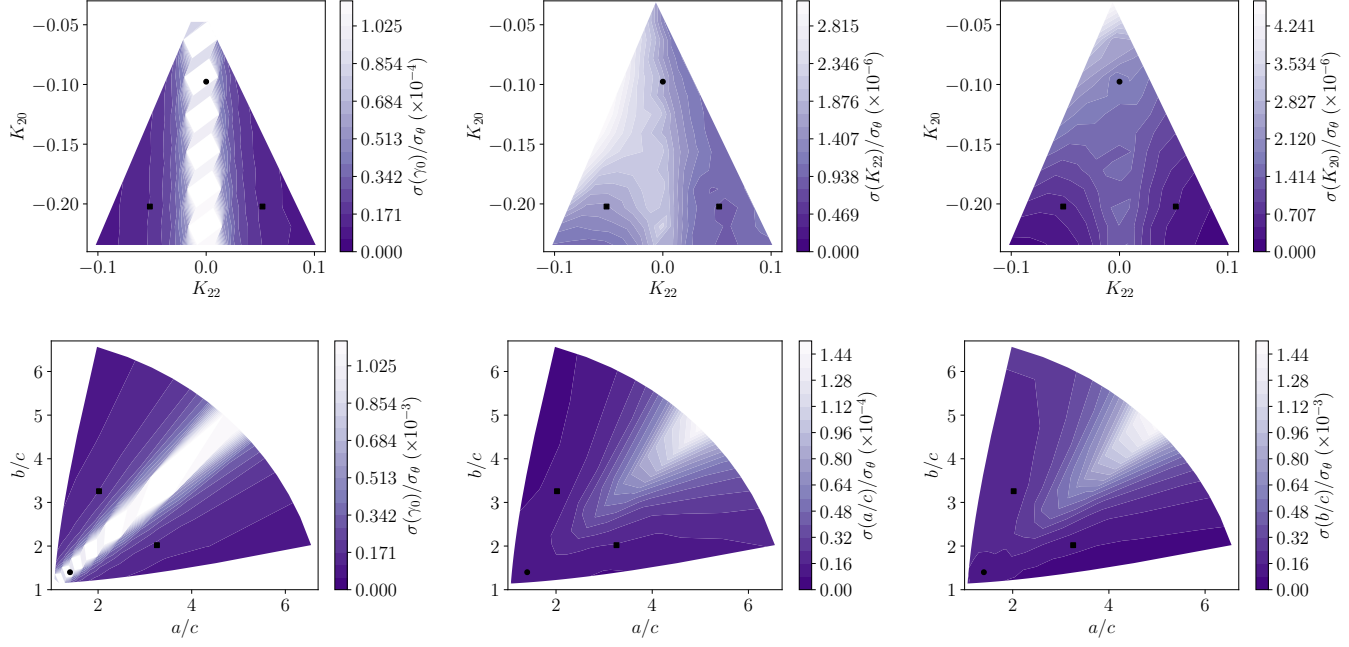


Figure 4. Ratios of fit uncertainties (the standard deviations of parameter posterior distributions) to experimental uncertainty (σ_θ) for fit parameters γ_0 , K_{22} , and K_{20} (top row) and γ_0 , a/c , and b/c (bottom row). Also shown are the reference asteroid shapes used elsewhere in this paper (appendix A); the symmetric case is marked with a circle and the asymmetric with a square.

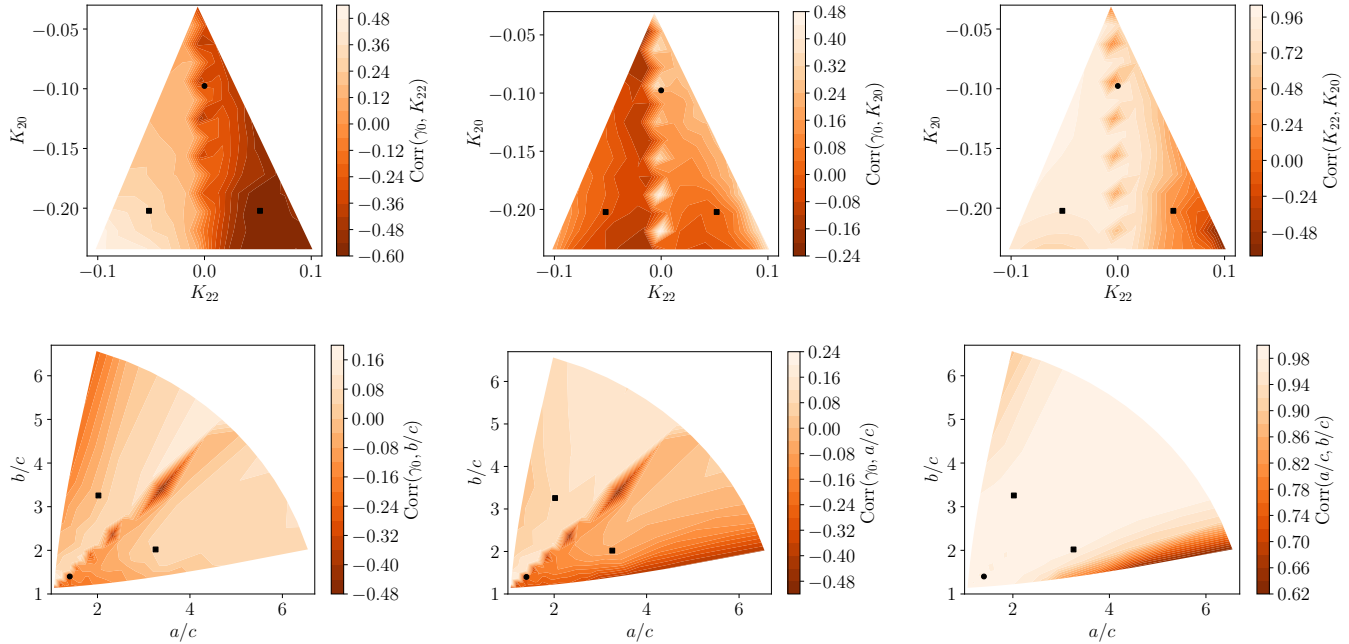


Figure 5. Correlations between fit uncertainties and experimental uncertainty (σ_θ) for fit parameters γ_0 , K_{22} , and K_{20} (top row) and γ_0 , a/c , and b/c (bottom row). Also shown are the reference asteroid shapes used elsewhere in this paper (appendix A); the symmetric case is marked with a circle and the asymmetric with a square.

Benchmark configurations	$\sigma(\gamma_0) / \sigma_\theta$	$\sigma(K_{22} [a/c]) / \sigma_\theta$	$\sigma(K_{20} [b/c]) / \sigma_\theta$	$\text{Corr}(\gamma_0, K_{22})$	$\text{Corr}(\gamma_0, K_{20})$	$\text{Corr}(K_{22}, K_{20})$
Symmetric: $a = b$	36	1.9×10^{-6}	1.7×10^{-5}	-0.40	0.36	0.19
	36	9.4×10^{-5}	1.9×10^{-4}	-0.42	-0.29	0.96
Asymmetric: $a < b$	1.6×10^{-5}	1.5×10^{-6}	5.4×10^{-6}	0.32	-0.0053	0.88
	1.6×10^{-5}	9.4×10^{-5}	1.8×10^{-4}	0.082	-0.019	0.99
Asymmetric: $a > b$	1.5×10^{-5}	9.1×10^{-7}	4.8×10^{-6}	-0.58	0.017	0.15
	1.5×10^{-5}	1.5×10^{-4}	1.0×10^{-4}	-0.049	0.061	0.98

Table 1. Values for the standard deviation and correlation of γ_0 , K_{22} , and K_{20} (top entry of each row) or γ_0 , a/c , and b/c respectively (bottom entry of each row) for the symmetric and asymmetric reference points. The large $\sigma(\gamma_0)$ for the symmetric benchmark reflects the fact that γ_0 is not defined for a symmetric body, and the posterior probability distribution is poorly constrained.

γ_0 especially is large for $a \approx b \approx c$, which is the spherical case in which no tidal torque is generated. Beyond these two trends, uncertainty in a/c and b/c appear to scale linearly with these ratios.

Figure 5 demonstrates that the parameters are generally correlated. Specifically, γ_0 and $|K_{22}|$ are correlated for large $|K_{22}|$ which corresponds to highly asymmetric asteroids. Likewise, for the correlation of a/c and b/c with γ_0 . $\text{Corr}(\gamma_0, K_{20})$ is less, however. K_{20} and K_{22} are strongly correlated in general as are a/c and b/c .

Also shown in figures 4 and 5 are the reference asteroid configurations which we study when fixing the asteroid shape and varying other parameters. We note that these reference configurations capture the above trends in variance and correlation, so that they can be viewed as representative of all but the most extreme asteroid configurations. The measured values of variance and covariance are displayed in table 1.

4.2. Dependence on observational precision

Depending on the size of the asteroid, its orbital elements, and the availability of observation, uncertainty on the rotational pole of the asteroid is expected to vary between flybys. A detailed model of uncertainty in the rotational pole of the asteroid (a model that might simulate a full lightcurve, for example) is beyond the scope of this paper. However, in this section we demonstrate how the uncertainty in the fit parameters is governed by the observational uncertainty in rotational pole σ_θ and in the period σ_ρ as a rule-of-thumb to guide future investigation.

We represent $1-\sigma$ uncertainty in the fit parameters as the difference between the 84th or 15th percentile of the marginal posterior PDF for each fit parameter and its mean. For a multivariate Gaussian posterior PDF (which must also have Gaussian marginal PDFs), this $1-\sigma$ uncertainty is exactly the standard deviation of the marginal PDF. We perform a similar exercise for the $2-\sigma$ uncertainty.

We expect that high observational uncertainty corresponds to high uncertainty in the best-fit parameters. To show this trend, in figure 6 we plot the best-fit uncertainty as a function of the product of the two uncertainty types, with the ratio fixed at $\sigma_\rho/\sigma_\theta = 10^{-5}$ (the benchmark value) so that we are only sensitive to the total uncertainty. To check deviation from a linear trend, we plot the ratio of fit uncertainty to σ_θ . The figure shows no deviation from a linear trend except for high observational uncertainty, at which point the posterior distributions begin to fill the prior distributions and are no longer Gaussian.

To test the relative importance of σ_ρ and σ_θ , we also show best-fit uncertainty as a function of the ratio $\sigma_\rho/\sigma_\theta$ with the product fixed at $\sigma_\rho\sigma_\theta = 10^{-7}$ (the benchmark value) in figure 7. If σ_ρ and σ_θ were interchangeable in terms of their effect on precision of the posterior distributions, (e.g., if the experimental uncertainty were a function of $\sigma_\rho\sigma_\theta$ we might expect no dependence on the ratio of the uncertainties). However, we see relatively low uncertainty for low $\sigma_\rho/\sigma_\theta$ in figure 7, with roughly stable (or slightly decreasing) fit uncertainty for $\sigma_\rho \approx \sigma_\theta$. Therefore, for fixed product $\sigma_\rho\sigma_\theta$, low σ_ρ compared to σ_θ will yield more precise fits.

Due to the constancy of the ratio of fit to observational uncertainty for fixed $\sigma_\rho\sigma_\theta$, the ratio can be extracted for other asteroid configurations from figure 4, and we are not much concerned with the value of σ_θ used throughout this paper because we are aware that results can be easily rescaled.

4.3. Dependence on cadence

To analyze the degree to which our fit accuracy and precision depends on the rapidity of observation, we simulate a flyby of the reference asteroid with data taken at fixed intervals (“cadences”) of 2 minutes to one hour, perform a fit to each, and compare the precision and accuracy of the fit results as a function of cadence.

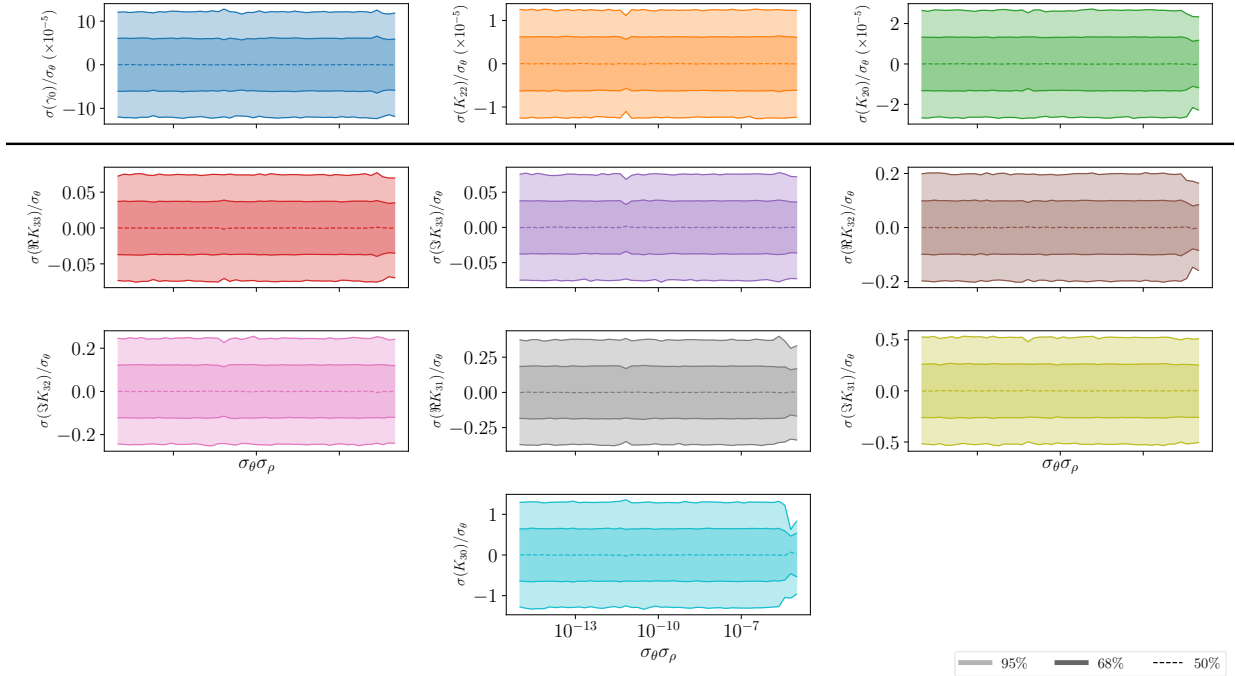


Figure 6. Ratio of 1- and 2- σ uncertainties of the marginal PDFs to the observational uncertainty σ_θ as a function of the product $\sigma_\theta \sigma_\rho$. A horizontal line divides the precise $\ell = 2$ parameters from the others. Except at large σ_θ , the ratio is observed to be constant. The asymmetric asteroid benchmark is used. Values of the ratio for other asteroid models can be computed from figure 4.

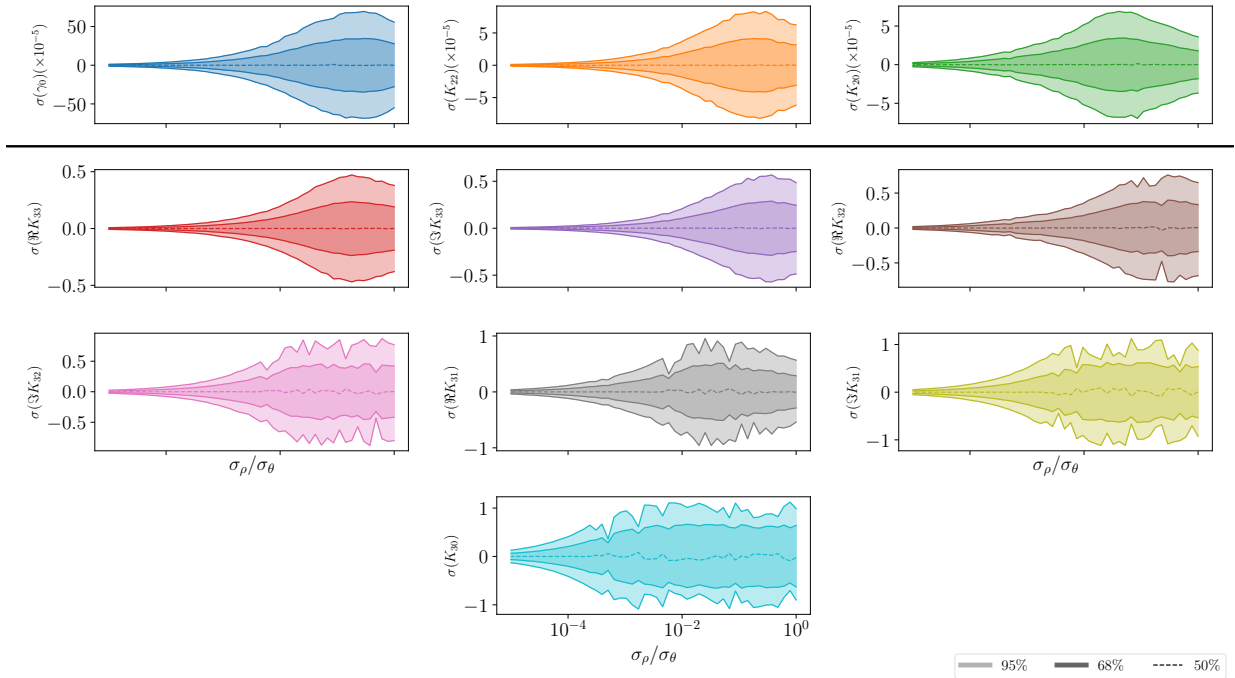


Figure 7. 1- and 2- σ uncertainties of the marginal PDFs as a function of the ratio $\sigma_\rho / \sigma_\theta$. A horizontal line divides the precise $\ell = 2$ parameters from the others. Period uncertainty σ_ρ is shown to be more vital than pole uncertainty σ_θ .

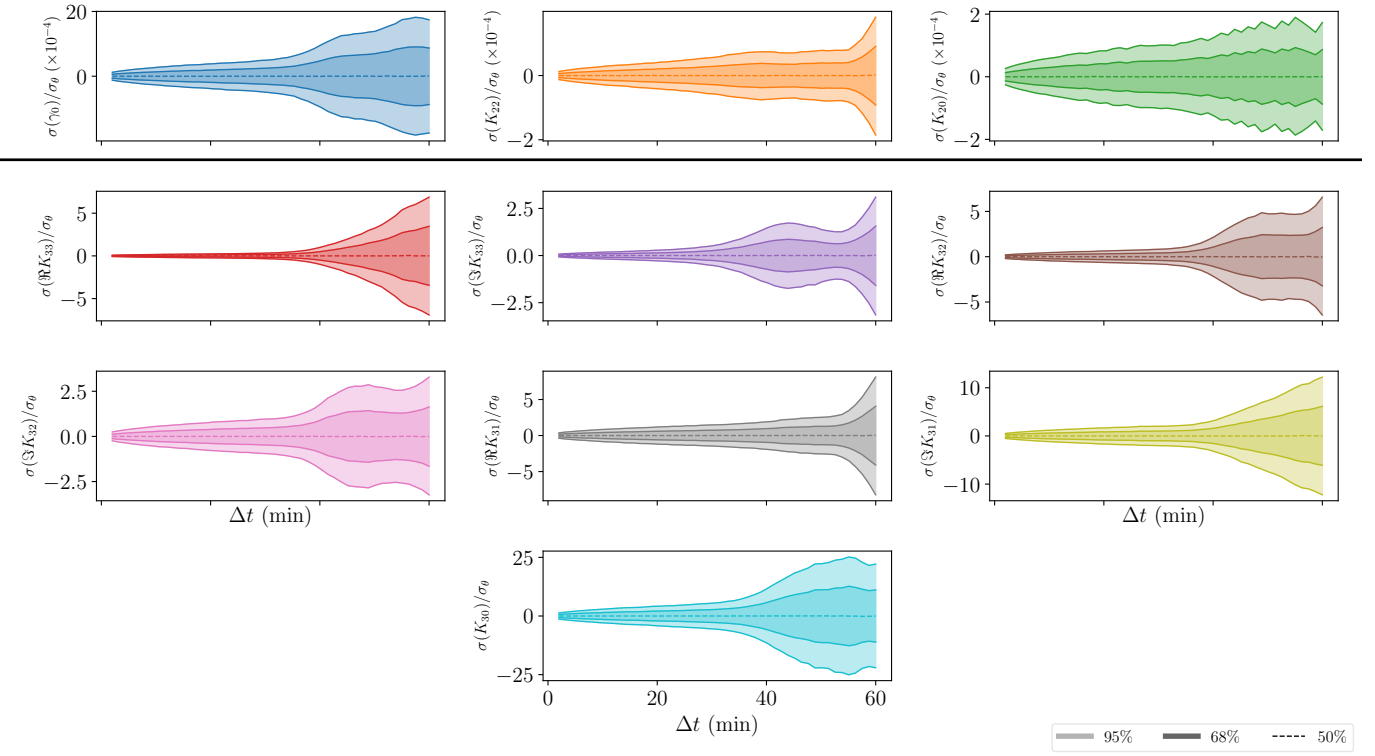


Figure 8. The 68th and 95th percentile envelopes for the posterior PDFs associated with ten fit parameters as a function of the cadence of the data set, plotted as a function of cadence.

Figure 8 shows the 68th and 95th percentiles of the posterior PDF for each fit parameter as a function of evenly-spaced cadences from 2 to 60 minutes. The percentiles are divided by σ_θ (which is constant in this figure) since they are expected to be linearly proportional to σ_θ in general. As expected, the precision of the fit result decreases with increased cadence (less data). However, the decrease is not uniform. All parameters show a slow increase in posterior PDF width until $\Delta t \approx 40$ min, at when a sharp increase PDF width occurs, often followed by a slight decrease before the uncertainty rises again. *Say more about this once the orbital information comes through.*

Figure 9 shows the difference between best fit parameter results and the true values as a function of cadence. No divergence is seen between then true and best-fit results for high cadence, demonstrating that even a small amount of data is sufficient to extract accurate parameters for the asteroid density distribution, albeit with the precision penalties shown in figure 8

4.4. Dependence on orbital parameters

The dependency of the best-fit parameter uncertainty on the orbit of the asteroid is analyzed in this section. We parameterize the orbit by v_∞ , the excess velocity, and r_p , the distance of the perigee. We do not change the plane of the orbit because this is equivalent to rotating J_{lm} , and since we use the benchmark model for this section (with a spherical planet) orbital plane changes have no effect.

Figure 10 shows the best-fit uncertainty divided by (constant) σ_θ as a function of v_∞ . The true K_{lm} parameters are extracted in all cases, generally with larger uncertainty for large v_∞ . This trend is in agreement with intuition, since flybys with larger v_∞ occur over a faster time range. Uncertainty in the high- and low-order parameters increases at a similar rate with v_∞ .

Figure 10 also demonstrates a strong dependence on the exact value of v_∞ through small-scale oscillations in precision as a function of v_∞ . This is because uncertainty is strongly dependent on the amplitude of oscillations after the encounter *how?*, and these oscillations are highly sensitive to initial conditions such as v_∞ .

4.5. Dependence on spin pole

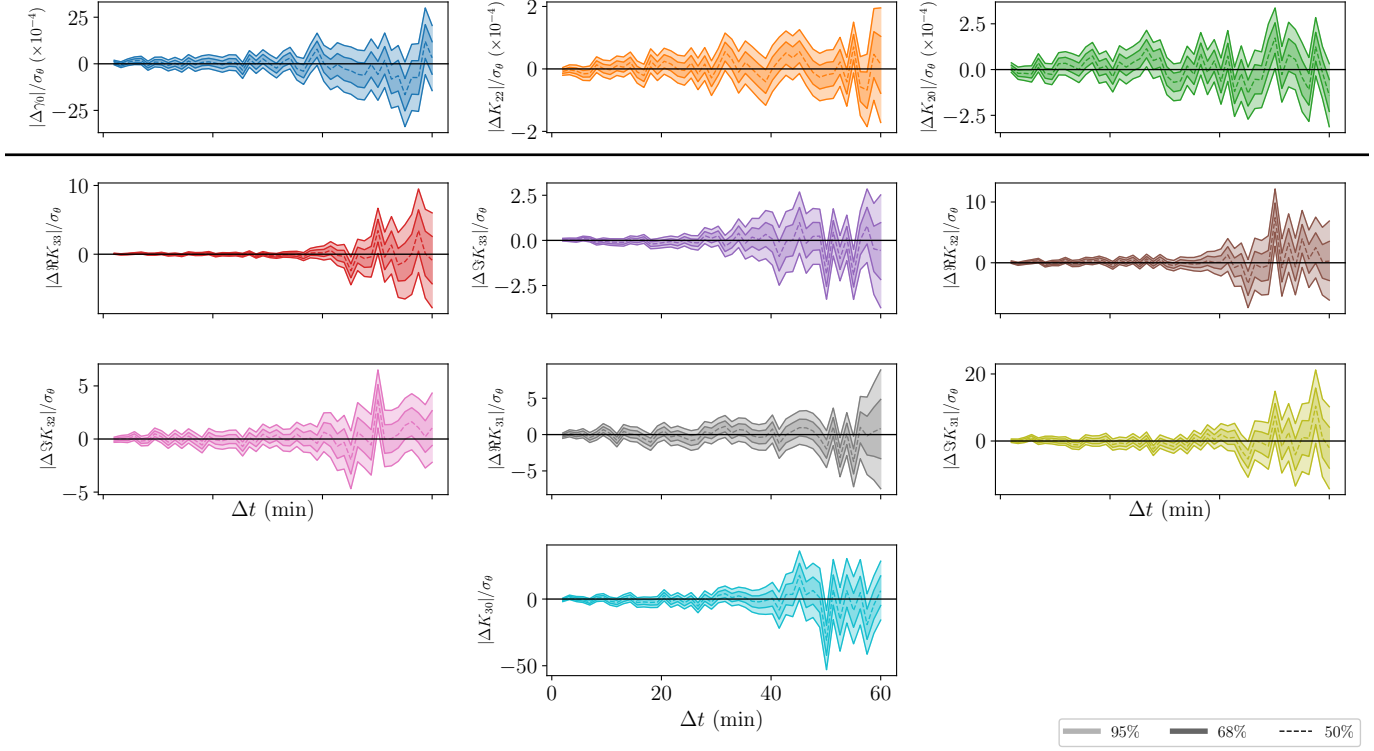


Figure 9. The difference between the fit parameters and the true parameters, with 68th and 95th percentile envelopes shown, for ten fit parameters as a function of cadence. No significant divergence is seen for high cadence. *Is this figure necessary?*

In addition to the physical parameters of the asteroid, the initial orientation of the asteroid spin pole strongly effects the precision of the best-fit parameters attainable from the data. For example, an asteroid with initial spin pole parallel to the orbital plane ($\beta = 0$) gives Wigner- D matrix elements $D_{mm'}^\ell \propto \delta_{mm'}$ and $D_{mm}^\ell = D_{-m,-m}^{\ell*}$. Note that the inner bracketed term of equation 22 transforms under $m \rightarrow -m$ as $[.] \rightarrow -(-1)^m [.]^*$. Since $S_{\ell m}$ and $D_{\ell m}$ transform to their conjugates and $J_{\ell m} \rightarrow (-1)^m J_{\ell m}^*$ while none of the other terms transform, the entire equation for tidal torque transforms to the opposite of its conjugate. Since τ is invariant under this transformation, which is equivalent to a rearrangement of terms, we must have $\tau = -\tau^*$. Since $\tau \in \mathbb{R}^3$, we have $\tau = 0$. Therefore the fit parameters $K_{\ell m}$ are entirely invisible when $\omega \propto \hat{Z}$ initially, and we expect to see decreasing fit precision near this limit.

Figure 11 displays the $1 - \sigma$ uncertainties on the first ten fit parameters of the asymmetric reference asteroid flyby as a function of the initial direction of the spin pole. In all cases, the asteroid's initial period was set to the reference 9 hours. The data is presented mapped onto a sphere which indicates the direction of the spin pole, in the Mollweide projection. To highlight common features between the ten parameters, the average standard deviation is presented in figure 12. The average is weighted such that the uncertainty map for each parameter contributes an equal amount (the weight of each is set to one-tenth of its mean). Also shown in 12 is the map of the average uncertainty with a polar projection, to show the high uncertainty near $\omega \propto \hat{Z}$.

To generate figures 11 and 12, the sphere was populated with 64 sample sites spaced on a Fibonacci sphere $(\theta_i, \phi_i) = (1 - (2i + 1)/64, 2\pi i / \varphi)$, where $\varphi \approx 1.618$ is the golden ratio. This yielded points that were roughly evenly distributed to avoid discontinuities in the figures. The locations of these 64 points are plotted in figure 12 for reference.

Figure 12 displays another point of lack of precision: that of $\omega \propto \hat{Y} + \frac{1}{2}\hat{Z}$. Not all of the parameters shown in figure 11 demonstrate this bare point, and some show lack of precision at $\omega \propto -\hat{Y} + \frac{1}{2}\hat{Z}$ as well. Better precision, however, was generally attained when aligning parallel or antiparallel to \hat{X} , the perigee vector. Initial poles with negative latitude also often relatively precise estimates. However, the average best-fit is not very volatile; it rarely grows to twice its mean over the sphere. Exactly which regions of the sphere yield better precision is likely controlled by particulars of the reference asteroid rather than fundamental properties of asteroid flybys, since no cases except when $\omega \propto \hat{Z}$ does $\tau = 0$.

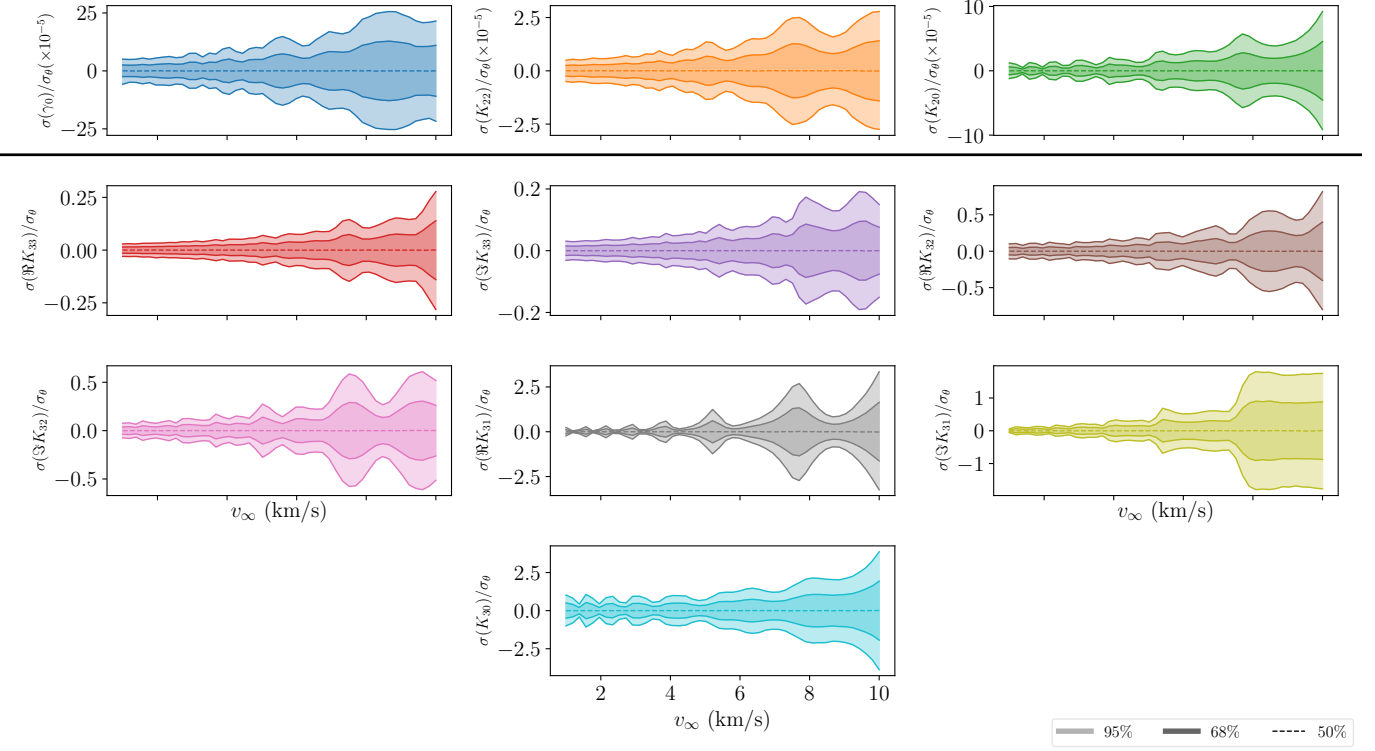


Figure 10. Best-fit uncertainties as a function of v_∞ , the excess velocity of the asteroid orbit. The three higher order parameters (top) are plotted with the seven lower order parameters. A general trend of increasing uncertainty for higher v_∞ is visible.

The increased uncertainty in the non-polar regions stems from the way the $K_{\ell m}$ are correlated. (If two $K_{\ell m}$ are highly correlated, we “double count” uncertainty because uncertainty in one parameter will yield uncertainty in the other). A metric of average uncertainty which is immune to correlation is the trace of the covariance matrix, since the trace of a covariance matrix transformed by an orthogonal matrix is the trace of the original covariance matrix. Note that this trace is also the sum of eigenvectors of the covariance matrix, which is the sum of the variances of uncorrelated parameters. This covariance matrix trace is plotted in figure ??.

4.6. Dependence on blocking out perigee

Much of the data available concerning an asteroid’s rotational velocity is captured long before or after the flyby perigee, where tidal torque is low. The angular velocity evolution here is dominated by torque-free precession dictated by the moment of inertia components, so that zero-torque data can still be used to fix K_{20} and K_{22} . However, K_{3m} are not extractable from precession data alone. We are therefore curious how much of the sensitivity of the system to K_{3m} components is due only to data taken during the encounter perigee.

To test this, we mask the perigee of the counter by removing data within time T of the perigee, where T ranges from 0 to 1 hour. To prevent lack of precision on $K_{\ell m}$ induced by lower amounts of data for high T , we always cut 1 hr – T from the beginning and end of the data set, so that all data sets produced for all T have the same length of data before and after the perigee. We then fit the same asteroid model to the cut data for all T and plot the standard deviations of the parameter posterior PDFs for (1) γ_0 and K_{2m} as a control, and (2) K_{3m} , to test whether they can still be fitted for without data concerning the perigee. We use the asymmetric benchmark asteroid configuration.

4.7. Oblate planet

Until this point, we have assumed an asteroid flyby of Earth because observations are most plentiful for near-Earth asteroids. However, it is worth considering how observations taken around another planet — by a large Earth-orbiting telescope or an interplanetary mission, for instance — could affect the efficacy of this model.

In particular, we consider how high planetary oblateness and the presence of moons affects the torque dynamics of asteroids. Other central body parameters worth of mention are the central body mass and radius. However, the

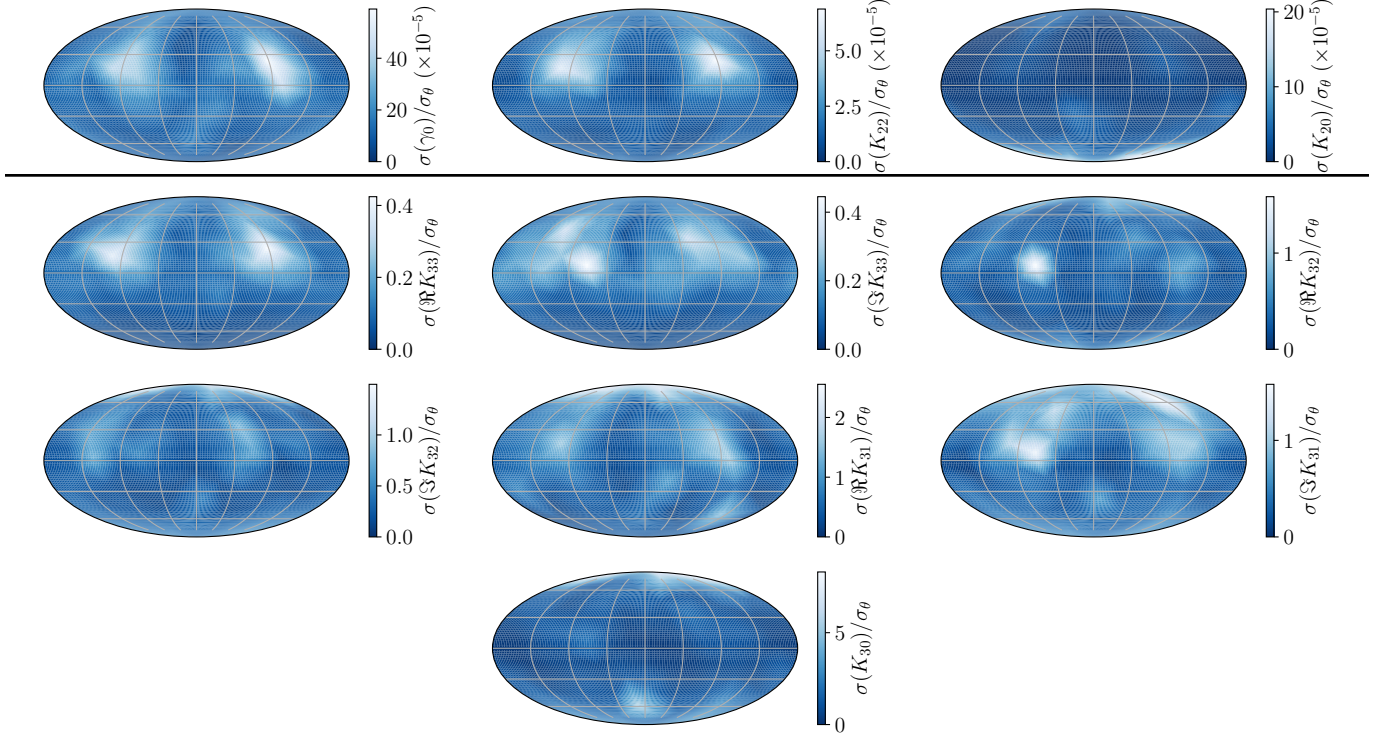


Figure 11. $1 - \sigma$ uncertainties in the first 10 asteroid fit parameters as a function of the initial direction of spin. All maps are made in the Mollweide projection and shown in the inertial $\hat{X} - \hat{Y} - \hat{Z}$ frame.

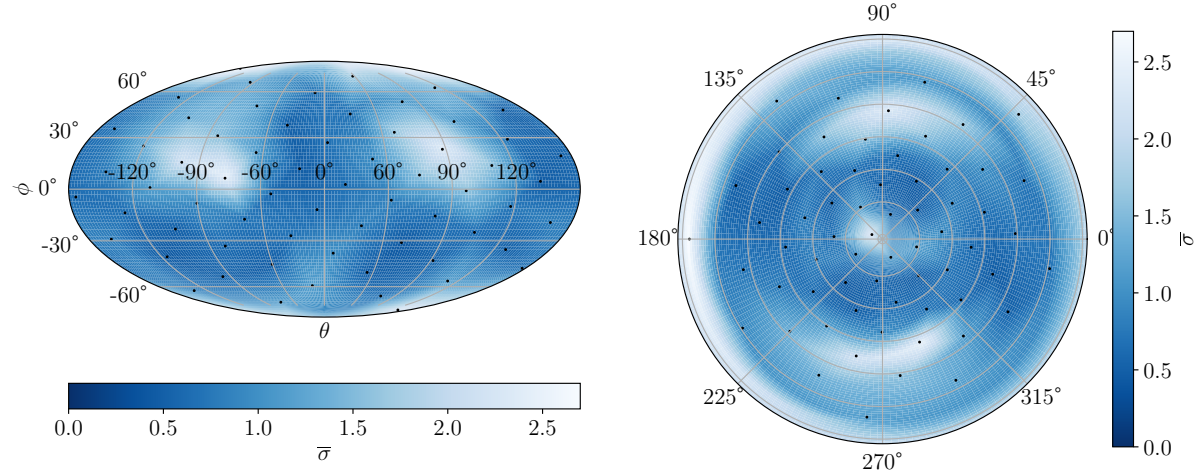


Figure 12. The weighted average of the uncertainties shown in figure 11, in Mollweide (left) and polar (right) projections. See text for a description of how the average was computed.

dependence of tidal torque on these properties is clear from equation 22 without requiring a simulation. If the central planet mass μ_M is increased, tidal torque increases uniformly and we expect greater precision in our measurements. If the planetary radius is increased, we also expect an increase in the distance D to the planet. Therefore, we consider changes in (a_M/D) . Each $J_{\ell m}$ term is multiplied by a factor of $(a_M/D)^\ell$, so an increase in planetary radius without a change in mass only affects the subdominant terms of 22.

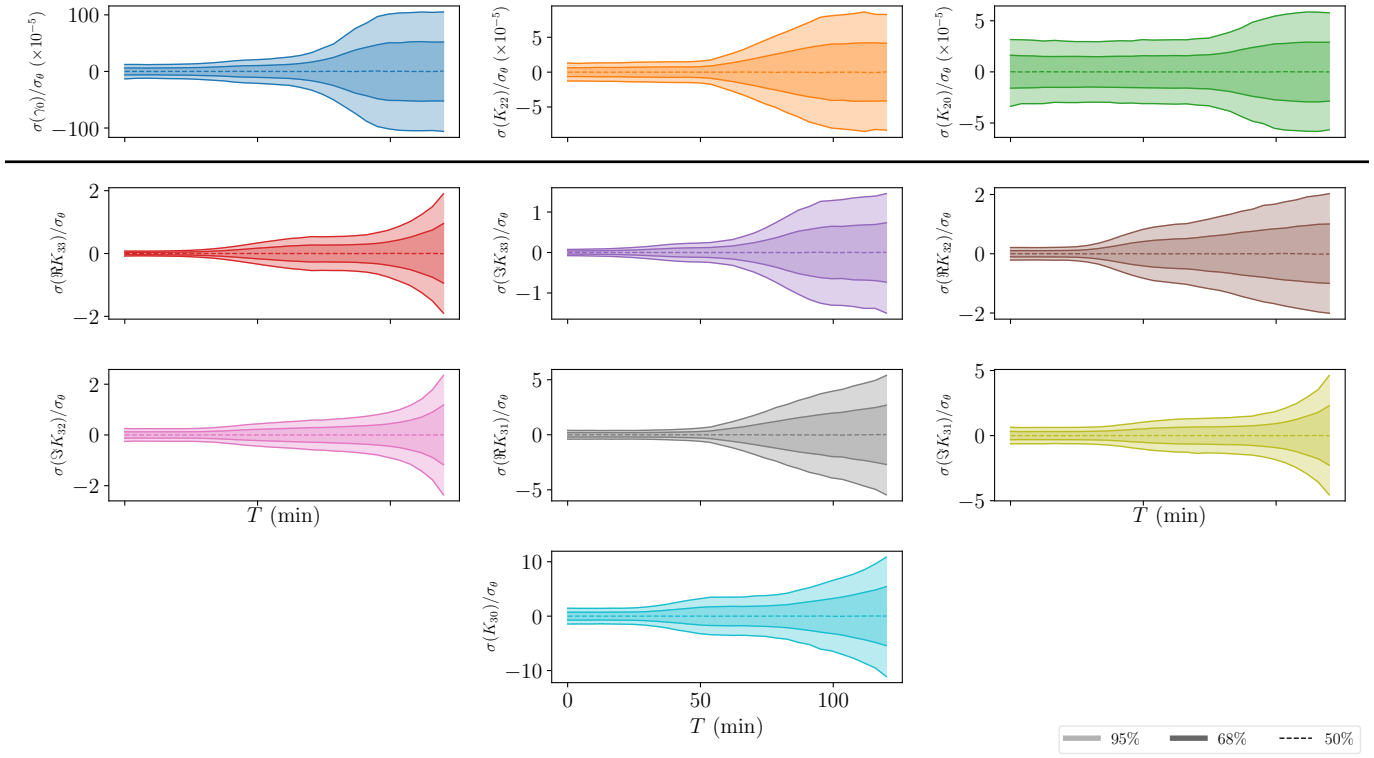


Figure 13. Observation gap

Depending on the composition and rotation rate of the planet which the asteroid is encountering, the oblateness (equivalently, the planet's J_{20} or J_2 value) may vary. The J_{1m} values are fixed at zero by the constraint that the center of mass of the central body must be at the origin. Equation 22 shows that the presence of a large J_{20} value introduces a second factor through which the K_{2m} parameters can affect the tidal torque, which is damped by an extra factor of D^{-2} compared to the J_{00} term. In this section, we ask what can be gained by a large oblateness.

Another factor work consideration is the presence of a planetary ring, which will affect J_2 . However, using the properties of Saturn's rings as an benchmark, we compute that the oblateness of the planet far outstrips the increase in J_2 caused by the ring, so we ignore this scenario henceforth. *Cite an appendix?*

For our purposes, we define oblateness to be $\epsilon = (I_z - I_x)/(\mu_M a_M^2)$ for central body moments of inertia $I_{x,y,z}$ where $I_x = I_y$ (that is, $J_{22} = 0$) and a_M is the true radius of the body, not the value defined in equation 25. (Some sources such as ? take this definition of ϵ as their definition of J_2 . Expressed in terms of $J_{\ell m}$, this is $\epsilon = -2J_{20}$. Given this conversion between ϵ and J_{20} , we generate simulated data sets and fit K_{2m} parameters to them for logarithmically spaced values of ϵ between 10^{-4} and 10^{-1} . The 68th and 95th percentiles deviations, computed as in figure 4, are shown in figure 14.

Figure 14 shows a slight dependence of best-fit uncertainty on oblateness, as expected due to the weakness of the J_{20} term in equation 22 compared to the dominant J_{00} term. However, the fit parameter uncertainty does slightly decrease as oblateness increases on further study. The trend of the decrease is linear, as shown by the close agreement between the overlaid best fit linear trend between the 1- and 2- σ best fit uncertainties to the measured values. We compute an average slope of the 1- σ trend divided by the uncertainty for zero eccentricity as $\Delta\sigma/\Delta\epsilon/\sigma_{\epsilon=0} = -0.25$ for γ_0 , -0.94 for K_{22} , and -1.2 for K_{22} . Other asteroid parameters K_{3m} will likely be affected by oblateness to similar degrees, however fitting these extra parameters is computationally more expensive.

The second figure of figure 14 shows divergence of best-fit parameters from the true values when an incorrect oblateness is used. Specifically, the figure shows the difference between parameter values extracted via a model with $\epsilon = 0$ and the true parameter values used to generate data with oblateness $\epsilon \neq 0$. The uncertainty on fit parameters is roughly constant over variations in ϵ_{true} , but very quickly (even for $\epsilon_{\text{true}} = 10^{-4}$) the fit values become inconsistent with the true values. The observational uncertainty used here was the benchmark value, but even if observational

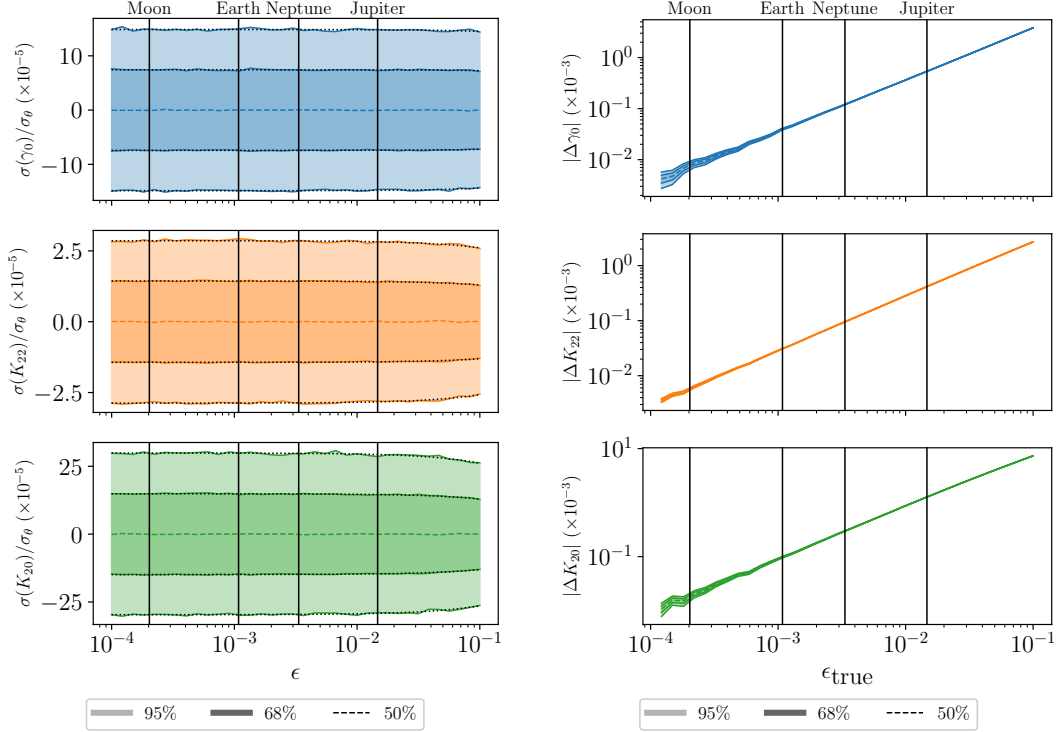


Figure 14. (Left) Ratio of 1- and 2- σ uncertainties of the marginal PDFs to the observational uncertainty σ_θ as a function of the oblateness ϵ of the central planet. Linear best fit lines (black, dotted) are plotted over the 1- and 2- σ uncertainties. (Right) The deviation of fit parameters from the true parameters when a zero oblateness model is fitted to data with oblateness ϵ . Also shown in both figures are the oblatenesses of reference Solar System bodies ?.

uncertainty were increased by a factor of 10 (resulting in a factor of 10 increase in best-fit uncertainty — see section 4.2) the figure shows that the best fit results would still exclude the true results by $> 2\sigma$ if the oblateness of Earth were approximated as zero. For 100-fold increase in uncertainty, mismodeling Earth’s oblateness would not lead to by 2σ divergence, but mismodeling Jupiter would.

Figure 14 also includes reference Solar System J_2 values listed in ? for comparison. However truly comparing these reference oblatenesses is complicated by the fact that the J_{20} term of equation 22 is modified by a factor of $(a_M/D)^2$. If the perigee of the orbit is fixed at the benchmark value of 5 planetary radii, we expect this term to remain roughly comparable between the different reference planets. However, if a_M/D increases for larger planet mass, which seems likely given that a larger planet presents a larger target, we expect the large-mass reference planets to show more dependence on oblateness than figure 14 suggests. In general, larger mass planets are gas giants and therefore have higher oblatenesses than rocky planets. Therefore, we expect more dependence on oblateness for gas giants.

5. INTERPRETATION OF THE FIT PARAMETERS

The previous sections have demonstrated that the parameters $K_{\ell m}$ can be extracted from a fit to spin data taken of an asteroid encounter given a_m . However, the most interesting physical property of the asteroid is the interior density distribution $\rho(\mathbf{r})$. Unfortunately, the density distribution is strongly degenerate given fixed parameters $K_{\ell m}$ and a_m . In this section, we outline four methods to extract density distributions under assumptions that reduce the degeneracy.

The first simplifying step we take is to extract $\eta(\mathbf{r}) = \rho(\mathbf{r})/\mu_m$ instead of $\rho(\mathbf{r})$ from $K_{\ell m}$ and a_m ; we do this because tidal torque data is not affected by the mass of the asteroid and the average density of the asteroid will therefore never be constrained. We further simplify matters by defining $H_{\ell m} = a_m^\ell K_{\ell m}$, so that the task is to find $\eta(\mathbf{r})$ such that

$$a_m^2 = \int_{\mathcal{A}} d^3 r \eta(\mathbf{r}) r^2 \quad H_{\ell m} = \int_{\mathcal{A}} d^3 r \eta(\mathbf{r}) R_{\ell m}(\mathbf{r}) \quad (45)$$

is satisfied with a_m^2 and $H_{\ell m}$ known. We made the shift from $K_{\ell m}$ to $H_{\ell m}$ because the constraints are now linear in $\eta(\mathbf{r})$; thus, if $\eta_1(\mathbf{r})$ and $\eta_2(\mathbf{r})$ both satisfy equation 45, then $(\eta_1 + \eta_2)/2$ does as well.

Equation 45 amounts to N constraints, when N values of $H_{\ell m}$ are known. This is because $H_{00} = 1$ by definition.

To resolve further degeneracy, we either assume (1) that the density η is constant and solve for the shape (section 5.1), or (2) that the shape is fixed and solve for $\eta(\mathbf{r})$. In the latter case, a further simplification is needed. We propose three models: one in which $\nabla^2 \eta = 0$ (section 5.2), one which averages over an ensemble of extracted distributions (section 5.3), and one which defines a likelihood on density distributions and find that which maximizes the likelihood (section 5.4).

5.1. Constant Density Model

Suppose our asteroid has constant density η_0 and known parameters $H_{\ell m}$ and a_m^2 , and that the asteroid is “star shaped” in that every point on its surface maps to a unique set of spherical coordinates θ, ϕ , and $r(\theta, \phi)$. We use the helpful identity

$$H_{\ell m} = \eta_0 \int_{\mathcal{A}} d^3 r R_{\ell m}(\mathbf{r}) = \eta_0 \int_{\mathcal{A}} d^3 r \nabla \cdot \mathbf{v}(\mathbf{r}) = \eta_0 \oint_{\partial \mathcal{A}} d^2 \mathbf{r} \cdot \mathbf{v}(\mathbf{r}) \quad (46)$$

where $\mathbf{v}(\mathbf{r}) = \hat{\mathbf{r}} R_{\ell m}(\mathbf{r}) r / (3 + \ell)$. We know the area element satisfies $d^2 \mathbf{r} = \partial \mathbf{r} / \partial \theta \times \partial \mathbf{r} / \partial \phi$ in our coordinates, and when dotted with $\mathbf{v} \propto \hat{\mathbf{r}}$, this gives

$$H_{\ell m} = \frac{\eta_0}{3 + \ell} \int_0^\pi d\theta \sin \theta \int_0^{2\pi} d\phi r(\theta, \phi)^3 R_{\ell m}(r(\theta, \phi), \theta, \phi). \quad (47)$$

The integrand of each $H_{\ell m}$ therefore is proportional to $r(\theta, \phi)^{(3+\ell)}$ times constants and a spherical harmonic. We can write $r(\theta, \phi) = \sum_{\ell m} Y_{\ell m}^* C_{\ell m}$ without loss of generality. To keep $r(\theta, \phi) \in \mathbb{R}$, we require $C_{\ell m}^* = (-1)^m (\ell - m)! / (\ell + m) C_{l,-m}$ so that the ℓ, m term of the sum for r is the conjugate of the $\ell, -m$ term.

With this definition of $r(\theta, \phi)$, equation 47 becomes a polynomial of degree $3 + \ell$ in terms of $C_{\ell' m'}$ and integrals of products of spherical harmonics. These integrals can be precomputed, since they are taken over the whole sphere $\theta \in (0, \pi)$ and $\phi \in (0, 2\pi)$. Equation 47 can then be numerically solved to get $C_{\ell m}$. To remove the degeneracy caused by the factor of η_0 , we evaluate $H_{\ell m} / H_{00}$ instead of $H_{\ell m}$. We also force the solution to reproduce the correct value of a_m^2 / H_{00} , calculated as

$$a_m^2 = \eta_0 \int_{\mathcal{A}} d^3 r r^2 = \frac{\eta_0}{5} \oint_{\mathcal{A}} d^2 \mathbf{r} \cdot \mathbf{r} (r^2) = \frac{\eta_0}{5} \int_0^\pi d\theta \sin \theta \int_0^{2\pi} d\phi r(\theta, \phi)^5. \quad (48)$$

5.1.1. Special Case: Constant Density Ellipsoid

Suppose that only $K_{\ell=2}$ are known. Then the above method is not necessary to compute the uniform density shape; we can assume the asteroid is an ellipsoid and solve for the axis lengths, which are

$$a = \sqrt{\frac{5}{3}} a_m \sqrt{1 - 2K_{20} + 12K_{22}} \quad b = \sqrt{\frac{5}{3}} a_m \sqrt{1 - 2K_{20} - 12K_{22}} \quad c = \sqrt{\frac{5}{3}} a_m \sqrt{1 + 4K_{20}}. \quad (49)$$

These arise out of computing the moments of inertia for a constant density ellipsoid and using equation 24 to relate the result to $K_{\ell m}$ and a_m . The values a , b , and c , represent semi-axes aligned with $\hat{\mathbf{x}}$, $\hat{\mathbf{y}}$, and $\hat{\mathbf{z}}$ respectively.

Again, the density of this asteroid cannot be extracted because, as is a general principle of gravitational interactions, the mass of the asteroid does not affect its dynamics. If a_m is unknown, the ratios a/c and b/c can be computed instead. Since I_{zz} is the greatest of the moments of inertia, we expect $a/c > 1$ and $b/c > 1$.

5.2. Fixed Surface $\nabla^2 \rho = 0$ model

Now suppose the shape of the asteroid is known, perhaps by a simplifying guess or perhaps by direct observation during a flyby. Then a density distribution $\eta(\mathbf{r})$ can be solved for which is consistent with observed values of $H_{\ell m}$ and a_m^2 . Supposing $\nabla^2 \eta = 0$, we write $\eta(\mathbf{r}) = \sum_{\ell m} C_{\ell m} R_{\ell m}(\mathbf{r})^*$. Thus, $H_{\ell m} = \sum_{\ell' m'} C_{\ell' m'} B_{\ell \ell' m m'}$ and $a_m^2 = \sum_{\ell' m'} C_{\ell' m'} v_{\ell' m'}$ where

$$B_{\ell \ell' m m'} = \int_{\mathcal{A}} d^3 r R_{\ell m}(\mathbf{r}) R_{\ell' m'}(\mathbf{r})^* \quad v_{\ell' m'} = \int_{\mathcal{A}} d^3 r R_{\ell' m'}(\mathbf{r})^* r^2 \quad (50)$$

can be precomputed due to the shape of \mathcal{A} being known. If we write $H_{\ell m}$ as a vector \mathbf{H} and similarly for \mathbf{C} , we can write $B_{\ell \ell' m m'}$ as a matrix B , obtaining $\mathbf{H} = \mathbf{BC}$. Combining this with the equation $a_m^2 = \mathbf{v} \cdot \mathbf{C}$, we get an

overdetermined matrix equation $\mathbf{d} = \mathbf{AC}$ where A is B with \mathbf{v} added as an additional row, and \mathbf{d} is \mathbf{H} with a_m^2 added. It follows that the density distribution coefficients that minimize the least squares distance between \mathbf{d} and \mathbf{AC} are

$$\mathbf{C} = \mathbf{A}^+ \mathbf{d} \quad (51)$$

where \mathbf{A}^+ is the Moore-Penrose pseudoinverse ?, defined by $\mathbf{A}^+ = \mathbf{A}^*(\mathbf{AA}^*)^{-1}$ where \mathbf{A}^* is the adjoint of \mathbf{A} .

Physically, there is no reason to expect $\nabla^2 \rho = 0$. However, the density distribution derived from the $C_{\ell m}$ s can be viewed as a projection from the true density distribution into the closest density distribution with $\nabla^2 \rho = 0$ everywhere, and therefore an approximation of the true distribution. This formulation for the density distribution of the asteroid is also conceptually useful because when \mathcal{A} is spherical, $B_{\ell\ell'mm'} \propto \delta_{\ell\ell'} \delta_{mm'}$. Thus, the fit coefficients $K_{\ell m}$ are proportional to $C_{\ell m}$, with proportionality constants governed by the values of $B_{\ell\ell'mm'}$ and a_m^ℓ . For a nearly spherical asteroid, small off-diagonal terms will be added to B , but we still expect $K_{\ell m}$ to roughly correspond to $C_{\ell m}$.

5.3. Fixed Surface Ensemble Average Model

Now we approach the problem of solving for the density distribution of an asteroid from $H_{\ell m}$ and a_m with more general assumptions. Suppose the shape of the asteroid is known, where “known” in this case means that an indicator function $\mathbf{1}(\mathbf{r})$ exists such that $\mathbf{1}(\mathbf{r}) = 1$ inside the asteroid and 0 elsewhere. Then we suggest a numerical algorithm to compute a representative distribution of the asteroid density distribution as follows.

1. Fill the asteroids with n uniformly random “seed points” by distributing them inside a bounding box containing the asteroid and rejecting those with positions \mathbf{r}_i such that $\mathbf{1}(\mathbf{r}_i) = 0$.
2. Construct n regions \mathcal{V}_i around each point such that the i th region is the set of all points inside the asteroid closest to the i th point. Suppose \mathcal{V}_i has uniform density ρ_i .
3. Equation 45 then becomes two linear equations $a_m^2 = \mathbf{v} \cdot \boldsymbol{\rho}$ and $\mathbf{H} = \mathbf{A}\boldsymbol{\rho}$ where ρ_i are the components of $\boldsymbol{\rho}$ and \mathbf{H} are $H_{\ell m}$ arranged as a vector. The components of \mathbf{v} and the matrix A are given by

$$v_i = \int_{\mathcal{V}_i} d^3 r r^2 \quad A_{(\ell m),j} = \int_{\mathcal{V}_i} d^3 r R_{\ell m}. \quad (52)$$

Precompute \mathbf{v} and A .

4. We can write equation 45 now as a matrix equation $\mathbf{d} = M\boldsymbol{\rho}$, where $M = A$ with \mathbf{v} added as an additional row, and $\mathbf{d} = \mathbf{K}$ with a_m^2 added in the corresponding entry. Thus, $\boldsymbol{\rho} = M^{-1}\mathbf{d}$ can be directly computed. Note that M is $N + 1 \times N + 1$, with the extra constraint enforcing that $\int_{\mathcal{A}} d^3 r \eta(\mathbf{r}) = 1$.
5. Go back to step 1 and compute new density maps with new draws of seed points. After sufficiently many computations, return the average of all the density distributions.

5.4. Fixed Surface Maximum Likelihood Finite Element Model

We present a final method to extract the density distribution of an asteroid with fixed surface and parameters $H_{\ell m}$ and a_m^2 . Suppose the asteroid is divided into N finite, constant density units with volume ΔV (a square grid, for instance). We further write the density of the i th unit as $\eta_i = C_i / \Delta V$, where C_i is a free real parameter. Approximating each unit as small, we may write

$$a_m^2 = \sum_i^N C_i r_i^2 \quad H_{\ell m} = \sum_i^N C_i R_{\ell m}(\mathbf{r}_i) \quad (53)$$

where \mathbf{r}_i are the centers of the units. Equation 53 is a matrix equation, which can be written in the form $\mathbf{d} = \mathbf{AC}$ where a_m and $H_{\ell m}$ have been arranged as a vector \mathbf{d} and \mathbf{C} contains the N values of C_i . The matrix A is non-square and cannot be inverted to find \mathbf{C} because equation 53 has many solutions. However, by imposing a probability distribution on \mathbf{C} , we find one configuration of \mathbf{C} that maximizes likelihood.

Suppose that the likelihood for \mathbf{C} is multivariate independent Gaussian distributed with each C_i having the same standard deviation. The log-likelihood is therefore $\ln \mathcal{L} \propto -(x - \mu)^2$. We expect that C_i sum to one by the definition of C_i , so we set $\mu = 1/N$. Thus, the value of \mathbf{C} we choose is the value which minimizes $|\mathbf{C} - \mathbf{1}/N|^2$, where $\mathbf{1}$ is an N -dimensional vector of only ones.

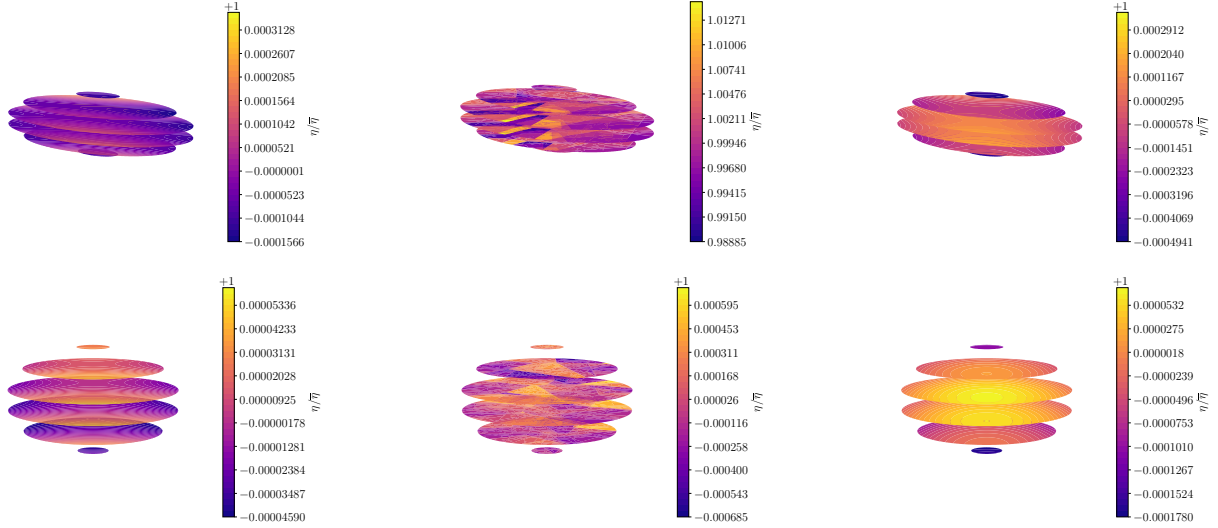


Figure 15. Density distributions extracted for the harmonic (*left*), ensemble average (*center*), and likelihood (*right*) models, with $K_{\ell m}$ values equal to the asymmetric (*top*) and symmetric (*bottom*) benchmark values, and ellipsoidal shapes equal to the shape of the associated constant-density ellipsoid. The same length scale is used in all six images.

This problem has already been solved in the context of the Moore-Penrose pseudoinverse. First, we define $\mathbf{k} = \mathbf{K} - \mathbf{A}\mathbf{1}/N$, so that if $\mathbf{k} = \mathbf{A}\mathbf{c}$, then $\mathbf{C} = \mathbf{c} + \mathbf{1}/N$ solves equation 53. We therefore attempt to minimize $|\mathbf{c}|^2$ to maximize the likelihood of density distributions.

The Moore-Penrose pseudoinverse of A is defined as $A^+ = A^*(AA^*)^{-1}$, where A^* is the adjoint of A ? The solution that minimizes $|\mathbf{c}|^2$ is $\mathbf{c} = A^+\mathbf{k}$.

5.5. Comparison of density distribution models

In this section, we compare the above methods of extracting asteroid density distributions given sample values for $K_{\ell m}$, to demonstrate their differences in behavior. To display the density distributions (and to derive them for the likelihood and ensemble average models), we subdivide the asteroid into a lattice of uniform-density cubes, each with a side length of ten meters. In the case of the ensemble average model, we average over 48 ensembles.

The sample $K_{\ell m}$ values we investigate are the symmetric and asymmetric benchmark values listed in appendix A. We execute the models for both benchmarks, and for the three models which require a fixed surface, we use both a spherical surface (radius equal to $\sqrt{5/3}a_m$) and an elliptical (axes set by section 5.1.1) model.

Figure 15 shows the density distribution produced by the three methods that fix the surface of the asteroid (the harmonic, ensemble average, and likelihood methods) for the symmetric and asymmetric benchmarks. Since the fixed shape is that of the constant-density ellipsoid associated with the same $K_{\ell m}$ s, we expect nearly constant density distributions. The harmonic and likelihood models produce the most uniform density distributions, with the likelihood model producing slightly less uniform distributions for the asymmetric case. The non-uniformity of the harmonic model appears to occur by extreme edges of the asteroid possessing different densities than the majority of the asteroid, whereas the likelihood model appears to establish a more radial gradient. The ensemble average shows a stochastic randomness of the density distribution throughout the asteroid.

In contrast, figure 16 shows density distributions extracted for spherical shapes with the asymmetric and symmetric benchmark $K_{\ell m}$ parameters. As expected, distinctly non-uniform densities are produced; indeed, negative densities are produced. For the ensemble average model, solutions with negative density regions could be discarded. But negative density values for the other two models are unavoidable without changes to the model, such as a different likelihood distribution for the density of each chunk.

Figure 16 shows that the harmonic and likelihood models produce very similar results *Is this because of non-uniformity in density or because of the spherical surface?*. The ensemble average value again produces a more noisy distribution.

In addition to these two shape constraints placed on benchmark asteroid parameters, we consider two asteroid shapes of note: a tetrahedron and a “dumb-bell.” These shapes are interesting because tetrahedral shape models for

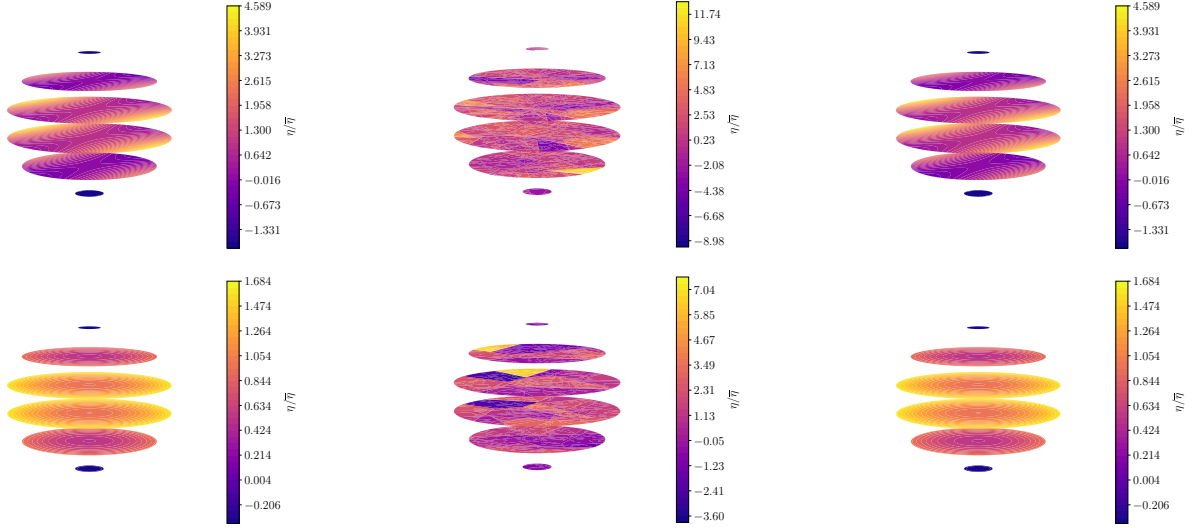


Figure 16. Density distributions extracted for the harmonic (*left*), ensemble average (*center*), and likelihood (*right*) models, with $K_{\ell m}$ values equal to the asymmetric (*top*) and symmetric (*bottom*) benchmark values, and spherical shapes with radius $r = \sqrt{5/3}a_m$. The same length scale is used in all six images.

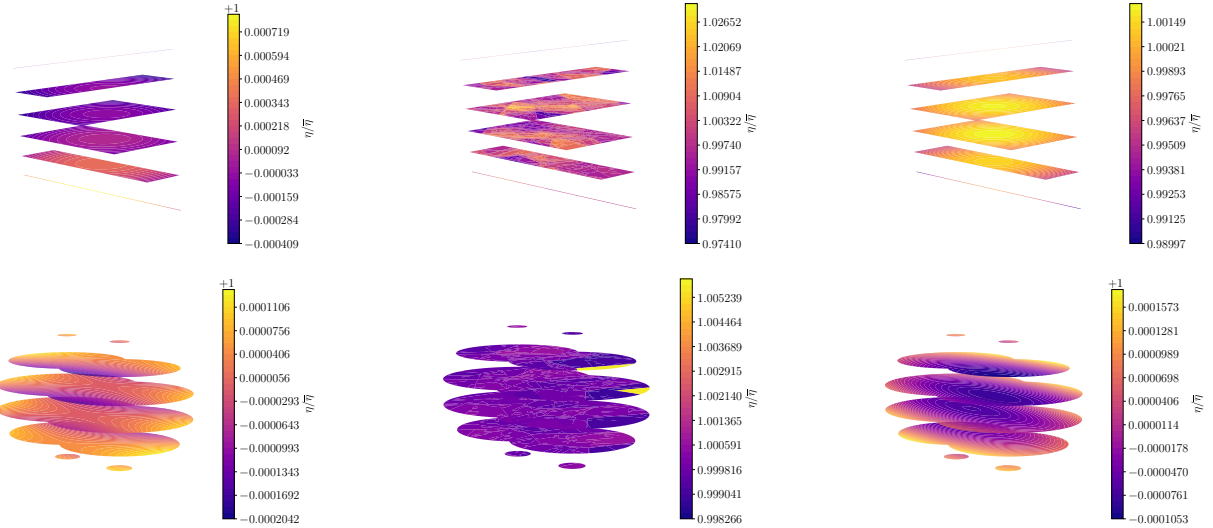


Figure 17. Density distributions extracted for the harmonic (*left*), ensemble average (*center*), and likelihood (*right*) models, with a tetrahedral asteroid shape (*top*) and a “dumb-bell” asteroid shape (*bottom*). $K_{\ell m}$ values were extracted assuming uniform density for both asteroids.

asteroids have hitherto been explored *Citation needed* and a dumb-bell shape can be taken as a proxy for a contact binary asteroid. The tetrahedron is composed out of four equilateral triangular sides and the dumb-bell consists of two spheres with radius r , separated by distance $r/2$. These shapes are fixed and values of $K_{\ell m}$ are calculated assuming constant density. Then the three shape models are run on the resulting $K_{\ell m}$ to reproduce the density distribution of the asteroid (figure 17). Once again, the harmonic and the likelihood models produce nearly uniform density distributions, with the ensemble method also producing a nearly uniform distribution. Similar to before, the likelihood model tends to show radial density distribution and the harmonic model tends to produce axial differences in density. All three models seem well suited for the both shapes.

Finally, we discuss the model which fixes constant density and solves for the asteroid surface. This model was run for the two benchmark $K_{\ell m}$ cases considered. A cutout diagram of the resulting density distribution is shown in figure

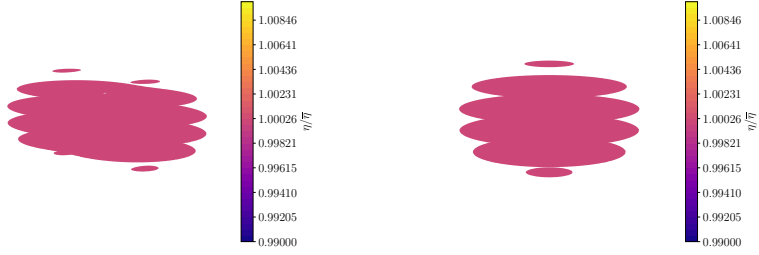


Figure 18. Density distributions extracted for the constant-density model, from the asymmetric (*left*) and symmetric (*right*) benchmark $K_{\ell m}$ parameters.

18. For the symmetric case, we see an ellipsoid of revolution closely resembling the true asteroid ellipsoid. For the asymmetric case, we see a two-lobed asymmetric formation with equal $K_{\ell m}$ to the asymmetric ellipsoid because a triaxial ellipsoid cannot be represented with spherical harmonics of degree $\ell \leq 2$. The model therefore takes the closest approximating route.

The figure demonstrates the limitations on the uniform density model: only a small number of shapes are accessible given fixed parameters $K_{\ell m}$ which may in fact be drawn from a diverse set of shapes from ellipsoids to tetrahedra to dumb-bells. However, a smooth shape distribution approximating the true distribution can nevertheless be fitted.

6. UNCERTAINTY TESTING

7. CONCLUSION

Facilities: MIT Supercloud

Software: emcee, scipy.optimize.minimize, numdifftools.Hessian

APPENDIX

A. REFERENCE FLYBY CONFIGURATIONS

Except when otherwise mentioned, we use the following fit parameters when running the simulation. Many of the parameter choices are made to maximize the quality of observations (a close orbit, large asteroid, etc.) This is so that if it is desired to test the dependence of fit results on perigee distance, for instance, the other parameters will not be fixed at values that are so unfavorable to observations that good fits are already excluded. Otherwise, the fit results for all perigee distances would always be poor and the dependence on perigee would be difficult to measure.

1. An orbit around Earth with 6 km s^{-1} excess velocity and perigee at 5 Earth radii. *Cite Apophis close approach*
2. An initial roll of $\gamma_0 = \pi/8$.
3. A cadence of 2 minutes and observational uncertainty of $\sigma_\theta = 0.01$ and $\sigma_\rho/\sigma_\theta = 10^{-5}$.
4. A rotational period of 9 hours, with the rotational velocity vector distributed between the $\hat{\mathbf{X}}$, $\hat{\mathbf{Y}}$, and $\hat{\mathbf{Z}}$ axes in a $1 : 2 : -2$ ratio.
5. An asteroid with radius $a_m = 1 \text{ km}$ and $K_{3m} = 0$. For K_{22} and K_{20} , we use two standard values. One with $(K_{22}, K_{20}) = (0, -0.097)$ and one with $(0.052, -0.202)$. Including the third point obtained by reflection $K_{22} \rightarrow -K_{22}$, these are the three points that minimize the mean distance between an arbitrary point in the allowed parameter space (equation 33) and these reference values. The first point is called the symmetric case because the corresponding uniform-density-ellipsoid model is rotationally symmetric around $\hat{\mathbf{z}}$. The second case and its reflection are called the asymmetric cases. Values of $(0.052, -0.202)$ have $a < b$ in the ellipsoid model, and the reflected value has $a > b$. If not specified, we use the $a < b$ case. Specifically, the asymmetric case has $a = 1839 \text{ m}$, $b = 1140 \text{ m}$, and $c = 565 \text{ m}$, while the symmetric case has $a = b = 1411 \text{ m}$ and $c = 1008 \text{ m}$.

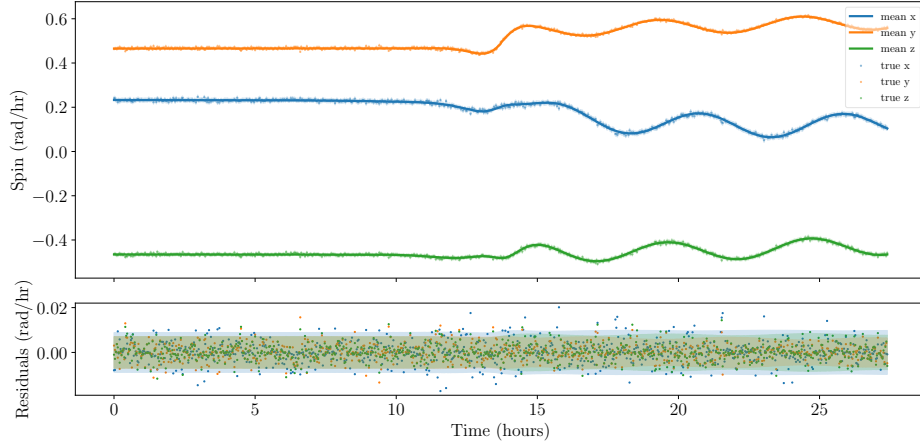


Figure 19. Data, best fit results, and residuals for a fit to synthetic data simulated for an asymmetric reference asteroid with $\sigma_\theta = 9.5 \times 10^{-3}$. The standard deviation of the data is plotted as an uncertainty band in the residuals plot, but these do not capture covariance between data points, so that the fact that many residuals lie outside the band does not disqualify the fit, which has a reduced χ^2 value of 0.68.

B. EXAMPLE FIT RESULTS

In the interest of demonstrating the result of a fit to synthetic data, we present the results of a fit to synthetic data generated with the nominal sensitivity model and $\sigma_\theta = 9.5 \times 10^{-3}$. The symmetric reference asteroid is used. The reduced χ^2 value of this fit (defined as χ^2/N , where N is the number of degrees of freedom) was 0.83, and fit results were in good agreement with the true parameters. Nearly 12,000 MCMC iterations were required before convergence.

Figure 19 shows the data with the best-fit overlaid and the residuals. Uncertainties are plotted on the residuals corresponding to the square root of the diagonal entries of the covariance matrix — i.e., $1-\sigma$ uncertainties. However, the data often exceeds these uncertainty bands. This is because uncertainties are correlated in truth, and points that fall outside of the band are not necessarily in conflict with the best fit.

Figure 20 shows a corner plot of the ten fitted parameters' posterior distributions, both marginalized to be a function of one variable and of two. The true parameters are shown as lines.

Figure 19 demonstrates that a good fit to data was achieved, despite the small error bars and strong dependence of the model on initial conditions. Figure 20 shows that the posterior distributions are largely Gaussian-distributed, with several of the parameters strongly correlated. The true values lie within 2σ contours in most cases, as expected. Parameters are computed to very high accuracy — $O(10^{-6})$ for γ_0 and $O(10^{-7})$ for K_{2m} (the first tier of parameters as ordered by the sensitivity of the asteroid system to their values), and $O(10^{-4}) - O(10^{-2})$ for K_{3m} . These ranges should be compared to the width of the prior distributions for these parameters, which is $O(1)$ for all. The success of this fit demonstrates that these higher order parameters can be fitted to data as long as good enough precision on the data is achieved.

REFERENCES

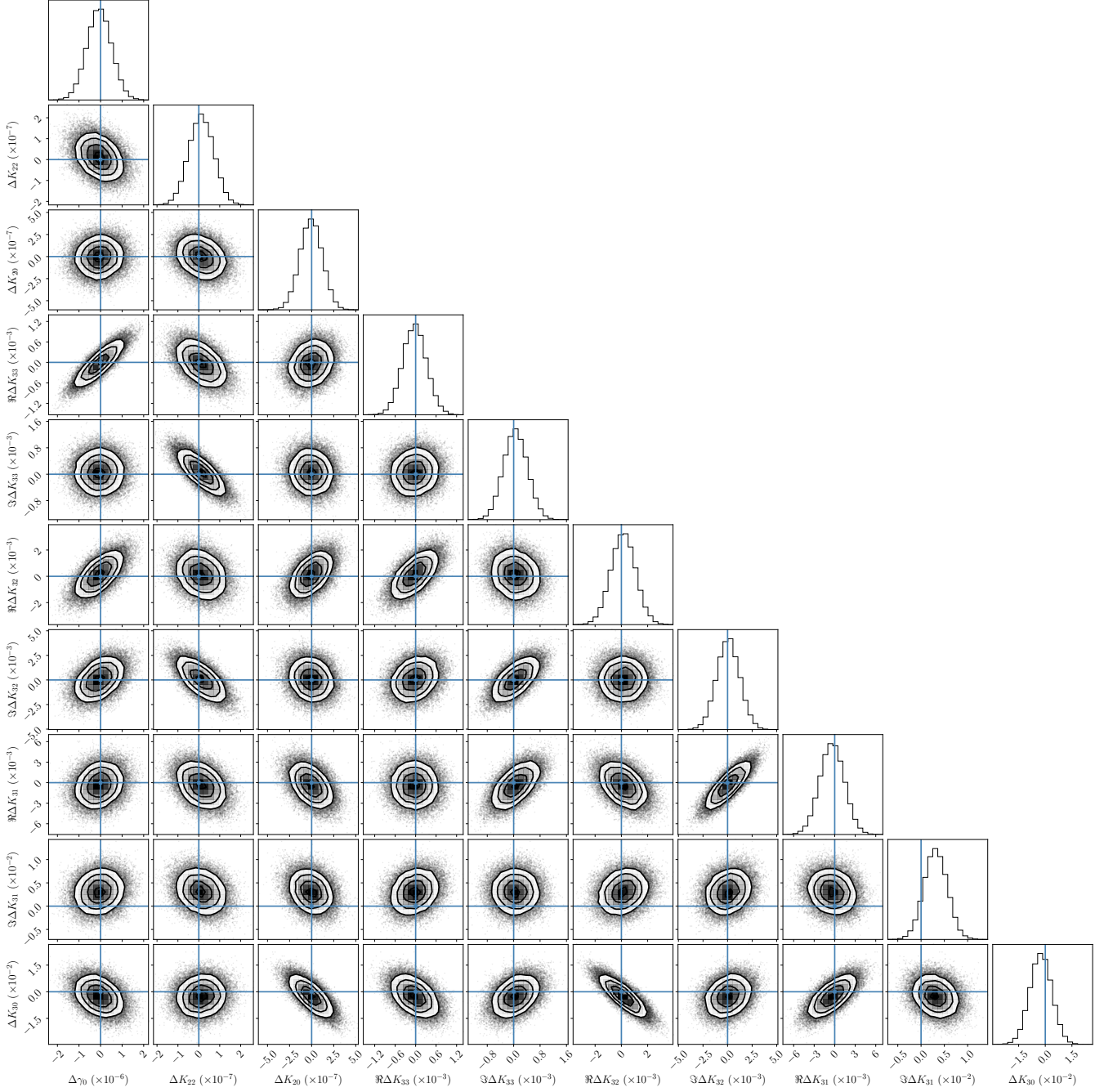


Figure 20. A corner plot for the fit results ten parameters to synthetic data simulated for an asymmetric reference asteroid with $\sigma_\theta = 9.5 \times 10^{-3}$. Marginal posterior PDFs for each parameter are shown (histograms) along with two-dimensional PDFs (contours). Individual points in the contours are samples from the MCMC fit, and the contours enclose 1-, 2-, and 3- σ of them. True values (which are zero here due to the parameters being displayed relative to the true values) are also shown (blue lines).